Research papers

Oscillations and trends of river discharge in the southern Central Andes and linkages with climate variability

Fabiana Castino *, Bodo Bookhagen, Manfred R. Strecker

University of Potsdam, Institute of Earth and Environmental Science, Karl-Liebknecht-Str. 24-25, 14476 Potsdam, Germany

A B S T R A C T

This study analyzes the discharge variability of small to medium drainage basins (10^2–10^4 km^2) in the southern Central Andes of NW Argentina. The Hilbert-Huang Transform (HHT) was applied to evaluate non-stationary oscillatory modes of variability and trends, based on four time series of monthly-normalized discharge anomaly between 1940 and 2015. Statistically significant trends reveal increasing discharge during the past decades and document an intensification of the hydrological cycle during this period. An Ensemble Empirical Mode Decomposition (EEMD) analysis revealed that discharge variability in this region can be best described by five quasi-periodic statistically significant oscillatory modes, with mean periods varying from 1 to ∼20 y. Moreover, we show that discharge variability is most likely linked to the phases of the Pacific Decadal Oscillation (PDO) at multi-decadal timescales (∼20 y) and, to a lesser degree, to the Tropical South Atlantic SST anomaly (TSA) variability at shorter timescales (∼2–5 y). Previous studies highlighted a rapid increase in discharge in the southern Central Andes during the 1970s, inferred to have been associated with the global 1976–77 climate shift. Our results suggest that the rapid discharge increase in the NW Argentine Andes coincides with the periodic enhancement of discharge, which is mainly linked to a negative to positive transition of the PDO phase and TSA variability associated with a long-term increasing trend. We therefore suggest that variations in discharge in this region are largely driven by both natural variability and the effects of global climate change. We furthermore posit that the links between atmospheric and hydrologic processes result from a combination of forcings that operate on different spatiotemporal scales.

© 2017 Elsevier B.V. All rights reserved.

1. Introduction

A recent study of river-discharge variability in the southern Central Andes of NW Argentina between 1940 and 1999 revealed a rapid change towards increasing discharge amounts that occurred between 1971 and 1977 (Castino et al., 2016), involving an up to 40% increase in annual mean discharge. This result is comparable to other investigations that showed a rapid increase in mean river discharge for large South American rivers (i.e., Amazon, Negro, Orinoco, La Plata, Paraná, Paraguay) during the 1970s (García and Mechoso, 2005; García and Vargas, 1998; Genta et al., 1998; Labat et al., 2004; Marengo, 2004; Pasquini and Depetris, 2010; Robertson and Mechoso, 1998).

The observed step change in river discharge was linked to the 1976–77 global climate shift that has been strongly impacting South American climate (e.g., Carvalho et al., 2011; Graham, 1994; Jacques-Coper and Garreaud, 2015; Kayano et al., 2009;

Miller et al., 1994). Coupled with this rapid change was a trend reversal in river discharge, with increasing (decreasing) values across (after) the change point, documenting the pronounced temporal variability of run-off in this region.

Although few previous studies addressed the possible causes of spatiotemporal rainfall and river-discharge variability in South America, the physical processes that drive changes in the hydrologic system have remained unclear (e.g., Antico and Kröhling, 2011; Antico and Torres, 2015; García and Mechoso, 2005; Marengo, 2004; Robertson and Mechoso, 1998).

The drivers for hydro-meteorological change in high-mountain catchments are complex, resulting in a pronounced non-stationary and non-linear character of the related hydrological processes (e.g., Compagnucci et al., 2000; Khaliq et al., 2006; Nourani et al., 2009). Most hydrologic studies in the Andean realm suggest that the El Niño Southern Oscillation (ENSO) exerts a first-order control on river discharge in major tropical and extra-tropical South American river basins. Alternatively, there are also investigations that document links between river discharge and the Pacific Decadal Oscillation (PDO) (Ferrero et al., 2015; Marengo, 2004)

---

* Corresponding author.
  E-mail address: castino@geo.uni-potsdam.de (F. Castino).

and/or the activity of the South Atlantic Convergence Zone (SACZ). It is important to note that most of these studies have particularly analyzed discharge variability for large catchments, such as the Amazon or La Plata river basins, which contain extensive floodplains, resulting in lag times that dampen the signals of discharge trends (Dunne and Mertes, 2007; Melack et al., 2009).

In light of these complex issues, we followed a three-tiered approach in our investigation: First, we identified magnitude and frequency of oscillatory modes at different timescales (1–20 y) that may explain river-discharge variability; second, we documented long-term discharge trends (>50 y); and third, we analyzed discharge linkages with large-scale modes of climate variability that affected climate in the southern Central Andes between 1940 and 2015. We used an innovative analysis combining the Ensemble Empirical Mode Decomposition (EEMD) (Huang et al., 1998; Huang and Wu, 2009) and the Time-Dependent Intrinsic Correlation (TDIC) (Chen et al., 2010). These methods are adaptive and are based on intrinsic information derived from the data; this approach is particularly appropriate for analyzing non-stationary geophysical time series that result from non-linear natural processes, providing not only the statistically significant intrinsic oscillatory modes that constitute the original time series, but also a statistically significant trend (Wu et al., 2007).

We relied on four time series of daily normalized discharge anomaly from 1940 to 2015 that were obtained from small to medium drainage basins (10^2–10^4 km^2) in the Eastern Cordillera of the Andes of NW Argentina between 21° and 26° S (Fig. 1). In contrast to the tropical and Patagonian Andes, there are virtually no glaciated peaks in this region (Lliboutry, 1998), resulting in a negligible contribution to streamflow from snow- and ice-melt compared to rainfall. Importantly, discharge from these catchment sizes is particularly sensitive to climate variability, because floodplain or groundwater reservoirs either do not exist or are very small compared to the more extensive drainage basins of the Amazon and La Plata rivers. In addition, we considered the monthly time series of four regional and global climate indices in the context of climate variability of the Pacific and Atlantic oceans. With the results of the EEMD analysis we subsequently identified the statistically significant intrinsic mode functions (IMFs) for discharge and climate indices. Also, for each pair of statistically significant IMFs of discharge and climate index the TDIC was estimated. Finally, the results of the TDIC analysis were used to decipher possible linkages between river-discharge variations in the southern Central Andes and large-scale climate modes of variability associated with the climate indices.

2. Geographic and climatic setting

With a length of approximately 7000 km, the meridionally oriented Andean orogen achieves elevations between 5 and 7 km asl and forms a hemispheric-scale orographic barrier for atmospheric circulation systems (Garreaud, 2009) (Fig. 1). Our study area comprises the low-elevation foreland, the steep eastern flank, and the eastern area of the high-elevation plateau region of the southern Central Andes between 21° and 26° S (Fig. 2). The foreland in the east is at about 0.5 km asl, whereas the high-elevation areas in the west reach peaks that are in excess of 6 km elevation. The western boundary of the study area encompasses the drainage divide of the internally drained Central Andean Plateau, the second largest plateau on Earth, with a mean elevation of about 4 km asl and low topographic relief. In contrast, the area between the foreland and the plateau constitutes a high-relief region of intermontane sub-Andean basins and ranges (Eastern Cordillera, Sierras Pampeanas and Santa Barbara ranges) with steep topographic gradients that are parallel to the border of the Andean Plateau.

The precipitation pattern in the southern Central Andes is controlled by the interaction between topography and hemisphere-scale atmospheric circulation patterns, resulting in a pronounced E-W climate gradient across the orogen (Bookhagen and Strecker, 2008; Campetella and Vera, 2002; Gandu and Geisler, 1991; Garreaud et al., 2010). Moisture transport along and into the southern Central Andes primarily occurs in the wet season during the austral summer and is an integral part of the South American Monsoon System (SAMS) (Marengo et al., 2012; Silva and Carvalho, 2007; Vera et al., 2006; Zhou and Lau, 1998). The onset of the SAMS is between September and October and typically lasts until the end of the austral summer/fall in March, generating the conditions for an efficient precipitation and erosional regime in the high Andes (Bookhagen and Strecker, 2012, 2008; Silva and Carvalho, 2007). Major features controlling moisture advection towards the subtropical regions of South America are the South American Low-Level Jet (SALLJ) and the South Atlantic Convergence Zone (SACZ) (Boers et al., 2015; Gandu and Silva Dias, 1998; Marengo et al., 2012), whose strength strongly affects the spatiotemporal variability of precipitation (Fig. 1b). In addition, on interannual timescales, the precipitation in the NW Argentine Andes may be modulated by the interplay between different atmospheric features, such as the Bolivian High (i.e., an upper-level (~200 hPa) anticyclone developing during austral summer over the Bolivian Altiplano), the Chaco Low and the North-Western Argentinian Low (low-level thermal depressions localized over these regions) (Boers et al., 2014; Carvalho et al., 2004; Gandu and Silva Dias, 1998; Salio et al., 2002; Schwerdtfeger, 1976; Seluchi and Saulo, 2003; Vuille and Keimig, 2004).

On average, about 80% of the annual precipitation on the eastern flanks of the NW Argentine Andes falls between November and February (Bianchi and Yañez, 1992; Garreaud et al., 2003, 2010; Halloy, 1982; Rohmeder, 1943). The rainfall gradient is mimicked by the distribution, type and density of vegetation cover (Jeffery et al., 2014). Consequently, subtropical forest vegetation along a narrow strip on the eastern flanks of the orogen is substituted by a sparse cover of xerophytes in the semi-arid to arid intermontane valleys farther west (Ruthsatz, 1977). In contrast, the western flanks of the orogen, the Andean Plateau, and the intermontane valleys in the lee of the outermost eastern ranges are semi-arid to hyper-arid (Bookhagen and Strecker, 2008; Garreaud et al., 2003).

The pronounced precipitation seasonality is reflected by the river-discharge annual cycle of the intermontane catchments, exhibiting homogeneous unimodal hydrographs with peak-discharge values between February and March (Castino et al., 2016; Pasquini and Depetris, 2007). A major river catchment originating in the study area is the Rio Bermejo (123 x 10^3 km^2 catchment size, 1060 km length), a tributary of the Rio Paraná, which is located in the second largest river basin in South America after the Amazon (Pasquini and Depetris, 2007).

In our study we will focus on the upper Rio Bermejo (50×10^3 km^2 catchment size), which constitutes small to medium-size catchments (10^2–10^4 km^2) located in the region encompassing the intermontane valleys (Fig. 2). These catchments, whose headwaters are at elevations above 4 km asl, are characterized by steep river gradients and variable climatic conditions that range from predominantly humid to semi-arid (Table 1). Along the course of these rivers, large amounts of sediments eroded from the hillslopes are transported, but often transiently stored in the intermontane valleys, before they are remobilized and further transported toward the foreland (COBINABE, 2010; Marcato et al., 2009). During the last decade, enhanced erosion from the orogen interior and transient sediment accumulation in the intermontane basins of NW Argentina have caused large flooding events, creating major problems to agriculturally-used lowlands and basic infrastructure maintenance, despite continual efforts to rebuild at higher levels (Cencetti and Rivelli, 2011; Marcato et al., 2012).
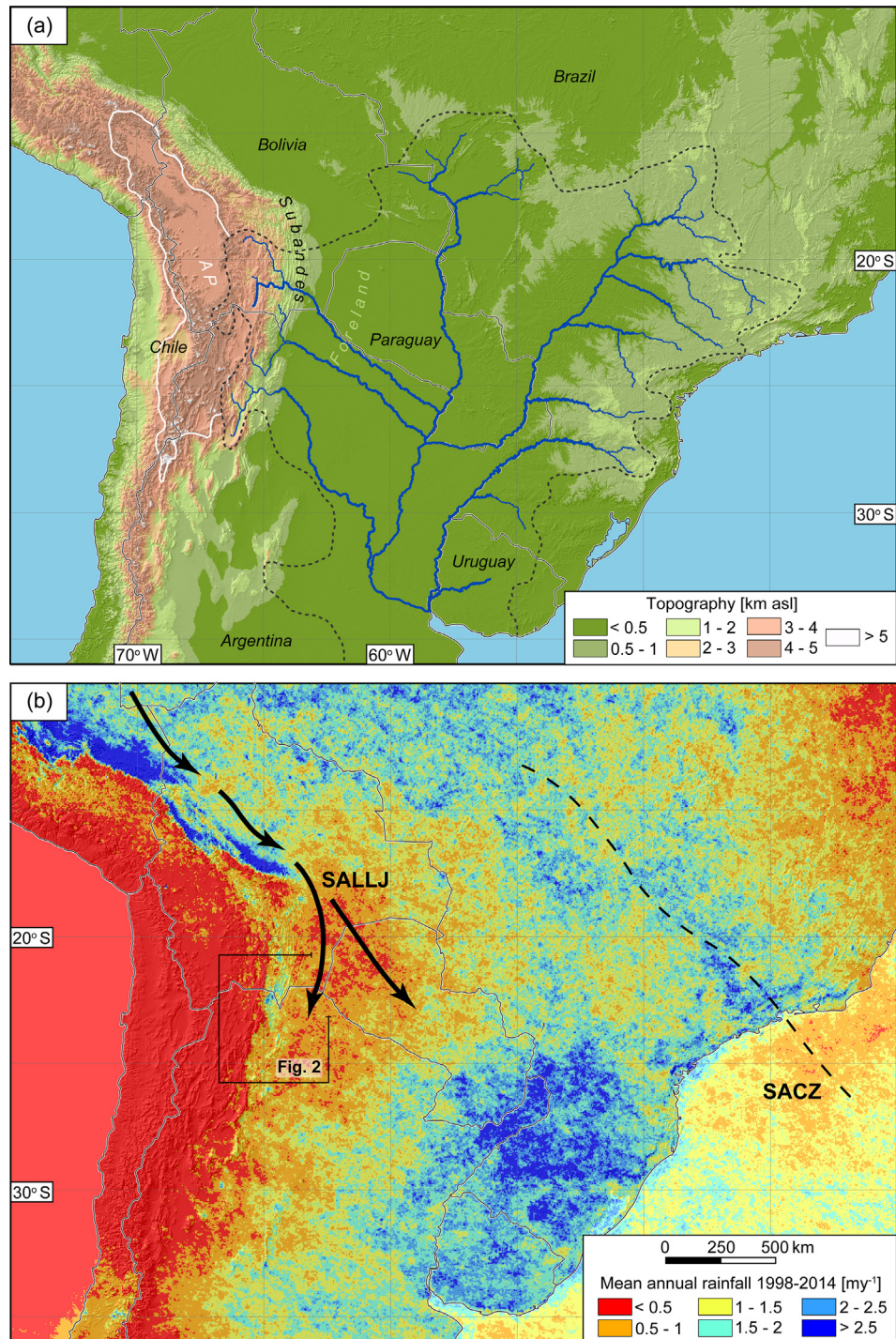
Fig. 1. (a) Topography (SRTM) of central South America. The catchments of La Plata River and the internally-drained Andean Plateau (Altiplano-Puna, (AP)) are outlined in dashed black and solid white lines, respectively; the thin light-grey line denotes international borders. (b) Mean annual rainfall data derived from TRMM 2B31 V7 (1998–2014) (Bookhagen and Strecker, 2008; Bookhagen and Burbank, 2010) and the main atmospheric features of the SAMS that control the rainfall pattern in subtropical regions (SALLJ and SACZ). Rainfall is characterized by a pronounced gradient between low-elevation frontal areas and arid, high-elevation areas of the internally-drained plateau in the orogen interior. The black rectangle delineates the study area in the Eastern Cordillera of the southern Central Andes of Argentina where discharge time series are available (cf. Fig. 2).

3. Data and methods

3.1. Data

Four time series of daily discharge were available for different time intervals starting from 1940 (Table 1). We analyzed two time intervals: (1) From September 1940 to August 2015 (75 y) with one

time series from the upper Rio Bermejo in Pozo Sarmiento (SA0693); (2) From September 1956 to August 2015 (59 y) with four time series from the upper Rio Bermejo: two from the main trunk at Pozo Sarmiento and Aguas Blancas (SA0604), and two additional ones from different tributaries (Rio Pescado at Cuatro Cedros, SA0629; Rio San Francisco at Caimáncito, JU0016) (Table 1).
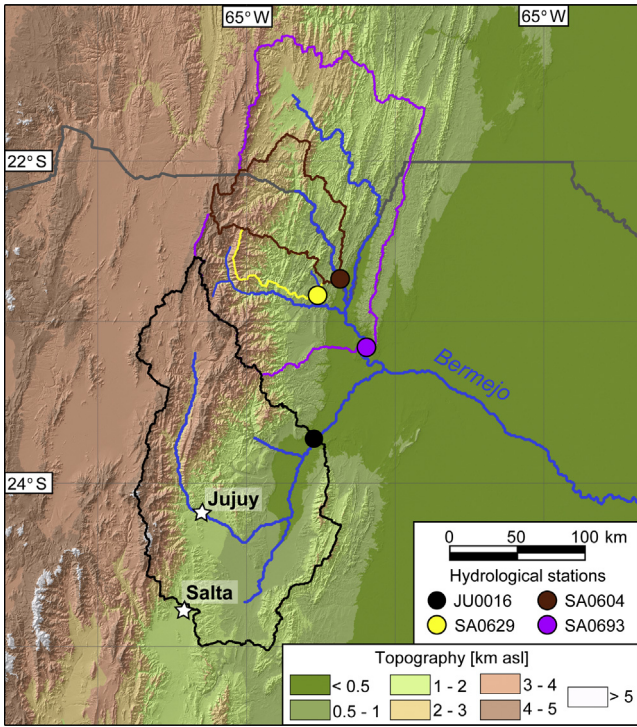
Fig. 2. Digital elevation model of the study area with principal drainages. Polygons represent the catchment areas at the station location and circles denote the four analyzed hydrological stations in the provinces of Jujuy and Salta. The white stars indicate the location of the cities of Jujuy and Salta. The grey lines indicate international boundaries.

We also considered four climate indices as proxies for large-scale coupled atmospheric-oceanic conditions: (1) the El-Niño Southern Oscillation BEST index (ENSO BEST, combining Nino 3.4 SST and the Southern Oscillation Index, Smith and Sardeshmukh, 2000); (2) the Tropical Southern Atlantic sea-surface temperature (SST) anomaly (TSA, SST anomaly is calculated in the box 30°W – 10°E, 20°S – 0°, Enfield and Mestas-Nunez, 1999); (3) the SunSpot Number index (SSN, Clette et al., 2014); and (4) the Pacific decadal Oscillation index (PDO, the leading EOF of mean November through March SST anomalies for the Pacific Ocean to the north of 20°N, Mantua and Hare, 2002). All climate indices, except the TSA, are available for the time interval between 1940 and 2015; the use of the TSA index was limited to the time interval between 1956 and 2015 (Table 2). All time series available for the time interval between 1940 and 2015 (normalized discharge anomaly and climate indices) are shown in Fig. 3 (see the Supplementary information for the time series relevant to the time interval between 1956 and 2015, Fig. S1).

3.2. Methods

3.2.1. Data preparation

First, the daily observations of discharge were converted into mean monthly discharge values. Short data gaps in the time series

Table 2
Time series for both normalized discharge anomaly and climate indices for the two considered time intervals between September 1940 and August 2015 (Fig. 3), and between September 1956 and August 2015 (Fig. S1).

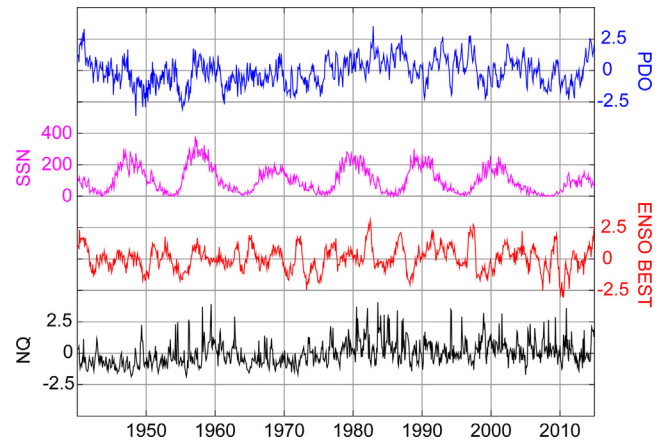|	Time interval 1940-2015	Time interval 1956-2015
Discharge time series	SA0693	SA0693, SA0604, SA0629, and JU0016
Climate indices	ENSO BEST, SSN, and PDO	ENSO BEST, TSA, SSN, and PDO

Fig. 3. Time series of the normalized discharge anomaly (NQ, SA0693, black), El-Niño Southern Oscillation BEST index (ENSO BEST, red) (Smith and Sardeshmukh, 2000), SunSpot Number index (SSN, magenta) (Clette et al., 2014), and the Pacific decadal Oscillation index (PDO, blue) (Mantua and Hare, 2002) for the time interval between 1940 and 2015.

of mean monthly discharge (at most 10% of data were missing) were filled using synthetic values obtained by standard linear regression with the time series of the neighboring station with the highest correlation coefficient (World Meteorological Organization, 2011). To attenuate the annual cycle, which is mainly controlled by the SAMS, deseasonalized time series were generated as follows:

$$x_i^k = \frac{(z_i^k - \mu_i)}{\sigma_i} \qquad (1)$$

where z_i^k is the original time series, with k = 1, … ,N_y, N_y is the length of the time series in years and i = 1, …, 12 is the month (i = 1 for Jan,…, 1 = 12 for Dec), and μ_i and σ_i are the monthly mean and standard deviation of discharge over the entire time-series length, respectively (Mcleod and Gweon, 2013; Wilks, 1995). We refer to the deseasonalized time series of discharge as *the time series of normalized discharge anomaly* (Table 2).

The time series (normalized discharge anomaly and climate indices) were subsequently decomposed using the Ensemble Empirical Mode Decomposition (EEMD, Wu et al., 2004; Wu and Huang, 2009), which is an enhanced Empirical Mode Decomposition (Huang et al., 1998). Subsequently, the link

Table 1
Hydrological stations and station metadata. Legend: Time series start/end: YYYY-MM-DD; Length: Time-series length [years]; Area = area of the drainage basin at the station location [km²]; basin-wide mean annual rainfall derived from TRMM2B31 (Bookhagen and Strecker, 2012, 2008); Minimum and maximum elevation values of each basin derived from SRTM data.

Code	Basin	Station	Time series start	Time series end	Length [y]	Area [km²]	Mean annual rainfall [mm]	Elevation range [m]
JU0016	San Francisco	Caimancito	1947-09-01	2015-08-31	68	22136	630	350-5900
SA0629	Pescado	Quatro Cedros	1956-09-01	2015-08-31	59	1972	1440	480-4530
SA0604	Bermejo	Aguas Blancas	1944-09-01	2015-08-31	71	4885	1280	400-5030
SA0693	Bermejo	Pozo Parmiento	1940-09-01	2015-08-31	75	23782	1080	300-5100

between normalized discharge and climate indices was analyzed using the Time-Dependent Intrinsic Correlation (Chen et al., 2010).

3.2.2. The Empirical Mode Decomposition (EMD)

The EMD is based on the assumption that a time series results from different intrinsic modes of oscillations, whose energy can be associated with different timescales. Each of these oscillatory modes is represented by an intrinsic mode function (IMF) constrained by the following conditions: (1) in the entire time series, the number of extrema and the number of zero-crossings must either be equal or differ by, at most, one; and (2) at any point, the mean value of the envelope defined by the local maxima and the envelope defined by the local minima is zero (Huang et al., 1998). The IMFs represent an *a posteriori*-defined basis, which is intrinsically non-linear and non-stationary in amplitude and frequency. This is in contrast with standard spectral decomposition generating *a priori* harmonic functions with constant amplitude and frequency.

The IMF are generated from an arbitrary time series $x(t)$ through a technique known as the 'sifting process', which can be summarized as follows:

1. all local extrema of $x(t)$ are identified; subsequently all local maxima are connected by a cubic spline to form the upper envelope; the same is done for all local minima to form the lower envelope. The upper and lower envelopes encompass all data between them. The mean of these two envelopes is a function of time and designated as $m_1(t)$. The difference $h_1(t)$ between $x(t)$ and the mean $m_1(t)$ is computed:

$$h_1(t) = x(t) - m_1(t) \tag{2}$$

2. $h_1(t)$ represents the proto-IMF, but it potentially does not satisfy the building constraints (new extrema may be generated due to changing the local zero from a rectangular to a curvilinear coordinate system (Huang and Shen, 2014)). Therefore, in the next step $h_1(t)$ is treated as it were the data:

$$h_{11}(t) = h_1(t) - m_{11}(t), \tag{3}$$

where $m_{11}(t)$ is the mean of the two envelopes generated from $h_1(t)$. The sifting process is repeated k times, until the number of zero crossings and extrema of $h_{1k}(t)$ function, defined as:

$$h_{1k}(t) = h_{1(k-1)}(t) - m_{1k}(t) \tag{4}$$

satisfy the following two conditions: (1) are equal or, at most, differ by one; (2) stay the same for S consecutive times. Here, a critical decision must be made: the stoppage criterion, i.e. the value of S. For a review of the different criteria historically used for determining S, we refer to the relevant literature (Huang et al., 2003, 1998; Huang and Shen, 2014); we point out that Huang et al. (2003) suggested S-values between 4 and 8 for optimal siftings. After defining the stoppage criterion, the first IMF is designated at k iteration $h_{1K}(t)$ of the $x(t)$ time series:

$$C_1(t) = h_{1k}(t) \tag{5}$$

corresponding to the finest timescale or shortest period component of the time series.

3. The residue $r_1(t)$:

$$r_1(t) = x(t) - C_1(t) \tag{6}$$

still potentially contains longer period variations. Therefore, $r_1(t)$ is treated as the new time series and the steps from 1 to 3 are repeated n times until the final $r_n(t)$ residue either is smaller than an *a priori*-fixed threshold or becomes a monotonic function from which no more IMFs can be extracted.

Once the EMD procedure is completed, the $x(t)$ time series can be represented as the sum of all IMFs and the final residue:

$$x(t) = C_1(t) + C_2(t) + \ldots + C_n(t) + r_n(t) \tag{7}$$

The residue is commonly interpreted as the long timescale trend (Wu et al., 2007). Importantly, the mean period $\bar{T}$ associated with each IMF is estimated dividing the length of the time series (expressed for example in years) by the semi-sum of the number of maxima and minima (Wu et al., 2004).

The two known limitations of the EMD method are mode-mixing and data-ends effect problems. The mode-mixing problem arises when a clear spectral separation of the modes is not attained (Huang et al., 2003, 1999). The causes of mode mixing are related to signal intermittency, generating not only aliasing in the time-frequency distribution, but also rendering the physical meaning of individual IMF ambiguous. A second important source of inaccuracy is generated at both ends of the time series, i.e. the data ends effect (Wu et al., 2011; Zeiler et al., 2013), such as in other decomposition methods (e.g., wavelet analysis, Torrence and Compo, 1998). To overcome these limitations, the Ensemble Empirical Mode Decomposition (EEMD) was introduced, defining the final IMF components of the $x(t)$ time series as the mean of an ensemble of IMFs obtained by N trials, obtained by adding white noise of fixed amplitude to the $x(t)$ time series (Wu and Huang, 2009). The level of white noise added to the signal in the EEMD method is not of critical importance, as long as the noise has finite amplitude (i.e., non-infinitesimal compared with the amplitude of the original signal) and there are a fair and large number of ensembles to cancel out each white noise contribution in a time-space ensemble mean (Wu and Huang, 2009). It is widely accepted that EEMD largely overcomes both the mode-mixing and data ends problems, greatly improving the consistency of the decompositions of slightly different pairs of datasets and reducing the uncertainties at the time series borders (Wang et al., 2012; Wu et al., 2011; Zhang et al., 2010). It is important to mention that, although these advances have resulted in satisfying the requirements of most practical applications, a rigorous mathematical foundation of the EMD technique, necessary for making the empirical approach more robust, is not available yet. Although much effort has been devoted to improving its mathematical foundation, the implementation of EMD is still empirical and *ad hoc* (Wang et al., 2010). However, since its introduction, EMD has been used in a wide range of applications, providing particularly useful insights in climate and atmospheric studies (Antico and Torres, 2015; Chang et al., 2011; Franzke, 2012; Massei and Fournier, 2012; Wilcox et al., 2013; Wu et al., 2008, 2007).

Here, we applied the EEMD for each time series (normalized discharge and climate indices) using equally populated ensembles of 200 members and a white-noise amplitude equal to 0.5 for standardized climate indices (ENSO BEST, TSA, and PDO) and to 20 for the non-standardized climate index (SSN) (Table 4 and Fig. 3).

3.2.3. Hilbert spectral analysis (HSA)

In addition, the Hilbert spectral analysis (HSA), was applied to each IMF mode to characterize the time-frequency distribution of the IMF mode, extracting the local frequency information (Huang et al., 1998; Huang and Wu, 2009). With this method, the analytical signal $\bar{C}(t)$ can be described using the Hilbert transform,

$$\bar{C}(t) = C(t) + j\frac{1}{\pi}P\int_{-\infty}^{+\infty}\frac{C(t')}{t - t'}dt' \tag{8}$$

Table 3

Summary of EEMD analysis for the normalized discharge anomaly NQ (hydrological station SA0693, Fig. 2 and Table 1), ENSO BEST, SSN, and PDO for the time interval 1940–2015. For each statistically significant IMF, the value of its mean period $\bar{T}$ [y] is indicated; no mean period values are indicated for non-significant IMFs.

	$\bar{T}$[y]			
	NQ SA0693	ENSO BEST	SSN	PDO
IMF1	–	–	–	–
IMF2	–	–	–	0.6
IMF3	1.0	1.3	–	1.1
IMF4	2.5	3	–	2.6
IMF5	–	6.1	–	5.2
IMF6	9.4	10.9	11.2	11.3
IMF7	21.6	25.9	–	25.7
IMF8	–	–	–	–

Table 4

Time-independent Pearson correlation values between the normalized discharge anomaly (NQ) for station SA0693 and the available climate indices for the time interval between 1940 and 2015, for the entire time series and each IMF match. Only statistically significant correlation values are shown (p < 0.05).

		ENSO BEST	SSN	PDO
NQ SA0693	Entire time series	–	–	0.086
	IMF3	0.111	–	−0.132
	IMF4	−0.176	–	−0.143
	IMF6	−0.186	–	–
	IMF7	0.178	–	0.639

where P is the Cauchy-principle value (Huang et al., 1998). Eq. (8) can be expressed also using the complex-valued analytic formulation, as:

$$\bar{C}(t) = A(t)e^{j\theta(t)} \tag{9}$$

where $A(t) = |\bar{C}'(t)|$ is the instantaneous amplitude and $\theta(t) = arctan\left(\frac{I(\bar{C}(t))}{R(\bar{C}'(t))}\right)$ is the instantaneous phase function (Huang et al., 1998; Huang and Wu, 2009). From Eq. (9) it follows that for each IMF the energy density is given by the mean square value of the instantaneous amplitude and the instantaneous frequency can be estimated as:

$$\omega(t) = \frac{1}{2\pi}\frac{d\theta(t)}{dt} \tag{10}$$

The Hilbert method provides a viable estimation of the instantaneous frequency (Huang et al., 2009), but alternative methods are also available, e.g., the direct quadrature and Teager energy operator (Huang et al., 2009).

The combination of the EMD and HSA is the Hilbert–Huang Transform (HHT) (Huang, 2005). We applied the HHT Matlab™ packages provided by Huang and Wu (2009), which include the statistical significance test.

3.2.4. Statistical significance test

The EMD method provides a dyadic filter bank through numerical experiments on fractional Gaussian noise and white noise (Flandrin et al., 2004; Wu et al., 2004). It has been also observed that the IMF components of pure white noise are normally distributed, their Fourier spectra are identical and the product of their energy density and the corresponding mean period are constant. These properties were used to develop the statistical significance test for IMFs obtained by EMD, to distinguish pure noise derived IMF components from IMF components with physically meaningful information (Wu et al., 2004). Once the significance level has been determined, the confidence intervals of the test are estimated applying EMD to Gaussian white noise in a Monte Carlo simulation, to generate the spread function of mean energy density as a function of the mean period for all IMFs components. Thus, an IMF component of a x(t) time series is statistically significant at the significance level, whenever its mean energy density (i.e., the mean

square value of the instantaneous amplitude, from Eq. (9)) lies outside the confidence interval obtained for pure white noise (Wu et al., 2004). In this study we applied the statistical significance test to determine whether the IMF components of the normalized discharge and the climate indices time series contain physically meaningful information at the 5% significance level.

3.2.5. The time-dependent intrinsic correlation (TDIC)

When applied to non-stationary noisy time series, the classical, time-independent definition of the correlation may distort correlation information between the signals and provide an unphysical interpretation (Chen et al., 2010; Hoover, 2003; Rodó and Rodríguez-Arias, 2006).

Alternatively, and consistent with the non-stationarity of the time series, the correlation coefficient can be estimated using a sliding window or a scale-dependent correlation technique. The estimation of the correlation between time series may use window sizes defined by the local characteristic scale given by the data itself. Recently, Chen et al. (2010) proposed to use the EMD to estimate an adaptive window to calculate the TDIC for denoised signals (IMFs).

The TDIC of each pair of statistically significant IMFs is defined as:

$$R_i(t_k^n) = Corr(C_{1,i}(t_w^n)C_{2,i}(t_w^n)) \tag{11}$$

at any t_k, where *Corr* is the correlation coefficient of two time series and t_w^n is the sliding window size, defined as follows:

$$t_w^n = [t_k - nt_d/2 : t_k + nt_d/2] \tag{12}$$

The minimum sliding window size for the local correlation estimation is chosen as $t_d = max(T_{1,i}(t_k), T_{2,j}(t_k))$ where $T_{1,i}$ and $T_{2,j}$ are the instantaneous periods $T = \omega^{-1}$, and n is any positive real number (Chen et al., 2010). We emphasize that TDIC is meaningful when applied to pairs of statistically significant IMFs with similar mean period. In addition, in this study the statistical significance of the TDIC values were evaluated using a Student's *t*-test at the 5% confidence level.

This method has been applied in several studies to characterize the relationship between different time series (e.g., Chen et al., 2010; Huang and Schmitt, 2014). Here we used TDIC to evaluate correlations between normalized discharge and the climate

indices. In addition, the Time-Dependent Intrinsic Cross-Correlation (TDICC) is estimated applying TDIC analysis with time-lags varying from 2 to 12 months to evaluate possible delays in response between the climate indices and the normalized discharge anomaly.

4. Results

The Hilbert-Huang Transform (HHT) analysis was applied to the normalized discharge anomaly and the climate indices for two time intervals: from 1940 to 2015, and from 1956 to 2015. In the following two sections, the results of our analysis will be presented for each of these two time intervals. Each section first presents the results of EEMD analysis applied to the time series of the normalized discharge anomaly, including the results of the Hilbert spectral analysis. Subsequently, EEMD outcomes obtained from the climate indices are presented. Finally, time-independent Pearson correlation and TDIC are shown for pairs combining both the entire time series and the IMFs of the normalized discharge anomaly and the climate indices.

4.1. Time interval from 1940 to 2015

Results for this time interval refer to station SA0693. The power spectrum of this time series was obtained using a standard Fast Fourier transform (Frigo and Johnson, 2005) and does not show large amplitudes, except for harmonics at periods between 20 and 30 y (Fig. 4a, right panel). EEMD resulted in eight IMFs and a residue (Fig. 4), among which four IMFs (IMF3 ($\bar{T}$ = 1 y), IMF4 ($\bar{T}$ = 2.5 y), IMF6 ($\bar{T}$ = 9.4 y), IMF7 ($\bar{T}$ = 21.6 y)) and the residual (monotonically increasing) were statistically significant at the 5% level (Fig. 5). The mean period $\bar{T}$ associated with each IMF is estimated in years, dividing the length of the time series (number of years) by the semi-sum of the number of maxima and minima (Wu et al., 2004).

We observed that the high-frequency modes of oscillation associated with intra-annual variability ($\bar{T} < 1$ y) are not significant (i.e., the noise component), despite that they account for a large amount of the discharge-anomaly variance ($\geq$25% for each mode). In addition, although the time series were deseasonalized, up to 27% of the variance is explained by IMF3, relevant to the annual cycle ($\bar{T} = 1$ y). The remaining variance of NQ can be explained by IMF4 (17%) and by IMF6 and IMF7 (11% and 10%, respectively).

The instantaneous frequencies associated with the statistically significant IMFs were nearly constant and close to their mean value. In addition, local oscillations or 'spike-like' features around the mean value were also observed (e.g., instantaneous frequency of IMF4 in 1975, Fig. 4b right panel). Recalling that the frequency is defined as the derivative of the instantaneous phase (Eq. (10)), these spike-like features of the frequency explain the local phase
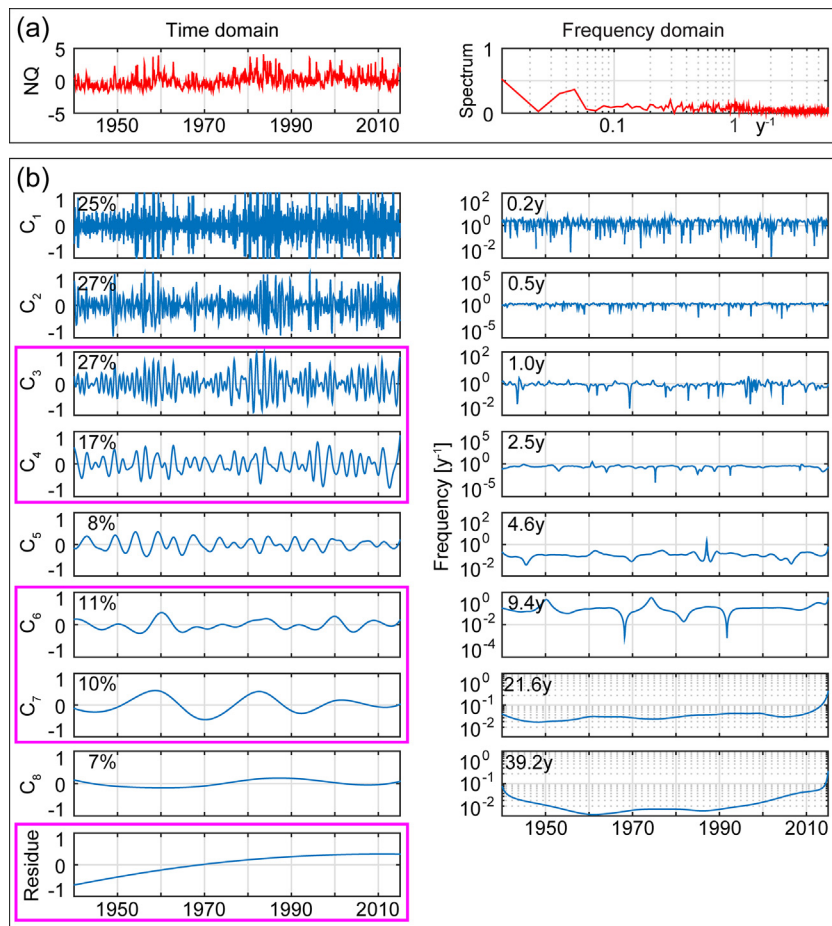

Fig. 4. (a) Monthly normalized discharge anomaly for hydrological station SA0693 (left) and the amplitude of its Fourier spectrum [s^{-1}] obtained applying a Fast Fourier transform (right). (b) IMFs obtained applying the EEMD method to the monthly normalized discharge anomaly (left). Eight IMFs and one residue have been obtained. Magenta rectangles indicate statistically significant IMFs (c.f., Fig. 5). Percentage represents the explained variance for each IMF. Since the IMFs obtained by EEMD do not constitute a basis of non-independent elements, the sum of all IMF explained variances can be higher than 100%. The right panel shows the instantaneous frequency of each IMF obtained by HSA; mean period $\bar{T}$ for the whole time series (1940–2015) is also reported.
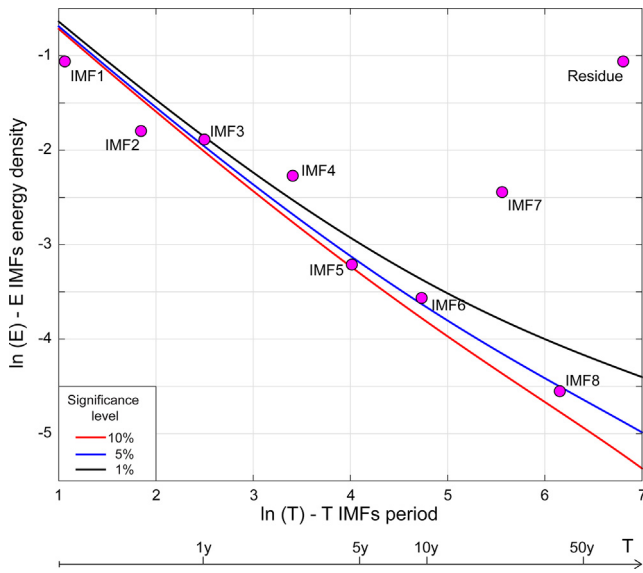
Fig. 5. Statistical significance test results for the IMFs of the normalized discharge anomaly (Fig. 4), based on the comparison between the energy density and spread functions obtained by white noise; lines correspond to the 90% (red), 95% (blue), and 99% (black) confidence interval superior extremes. Magenta circles represent energy density (i.e., mean square value of the instantaneous amplitude, from Eq. (8)) as a function of the mean period $\bar{T}$ (i.e., the ratio of the length of the time series (number of years) and the semi-sum of the number of maxima and minima) for each IMF (Wu et al., 2004). Each value above the blue line indicates an IMF that is statistically different from white noise at the 5% level. IMF3 ($\bar{T} = 1$ y), IMF4 ($\bar{T} = 2.5$ y), IMF6 ($\bar{T} = 9.4$ y), IMF7 ($\bar{T} = 21.6$ y), and the residue result to be statistically significant.

shift observed in the relevant IMF (e.g., C_4 in 1975, Fig. 4b left panel, and Supplementary information, Fig. S2). We observed that these oscillations were not synchronized for all IMFs. For example, for IMF4, the larger oscillation occurred during 1975, whereas for IMF6 two major oscillations of similar magnitude were observed in 1968 and 1992, respectively.

Importantly, we also observed that the amplitude of the oscillations of IMF3 of NQ strongly increased from the middle 1970s to the late 1990s (Fig. 6); to a lesser degree, a similar behavior was observed from the early 1950s to the middle 1960s. These local increases of IMF3 appeared to be synchronous, with one period of oscillation of IMF7, whereas the remaining IMFs did not exhibit similar changes (Fig. 6).

Monthly time series of ENSO BEST, SSN, and PDO for this time interval were also analyzed using EEMD. Table 3 and Fig. 6 summarize the statistically significant IMFs with the relevant mean period for each index, including normalized discharge anomaly. We observed that the ENSO BEST index was associated with five IMFs (IMF3-7), the SSN index with one IMF (IMF6), and the PDO index with six IMFs (IMF2-7). Individual results from EEMD, Hilbert spectral analysis, and statistical significance testing are documented in the Supplementary information (Fig. S3-8).

To evaluate possible links between the normalized discharge anomaly and the selected climate indices, we estimated the standard time-independent Pearson correlation for the complete time series as well as for each match of statistically significant IMFs (e.g., the match of IMF3 of NQ and IMF3 of both ENSO BEST and PDO) (Table 4). Low correlation values were found (absolute values of correlation less than 0.2), except for the IMF7 match between the normalized discharge anomaly (mean period $\bar{T} = 21.6$ y) and PDO (mean period $\bar{T} = 25.7$ y) ($\rho = 0.639$) (Table 3 and Table 4).

In a second step, the TDIC analysis was applied. As an example of the TDIC analysis outcome, the correlation obtained for the IMF4

(mean period $\bar{T} \approx 3$ y) pair of ENSO BEST and PDO indices is shown (Fig. 7). TDIC values for sliding window sizes smaller than the maximum instantaneous period of both two IMF4 at each time position were considered non-significant (i.e., at least one full cycle of the longest local wave length must be completed to consider the correlation between the two IMFs as significant). The TDIC plot results in a triangle whose base is defined by the length of the time series. Consequently, the top point corresponding to the maximum sliding-windows size represents the correlation coefficient between the two IMF4 for the whole time interval (from 1940 to 2015). In general, TDIC transitions from high to low absolute values as well as sign switches suggest potentially weakened physical mechanisms that link the analyzed processes (Chen et al., 2010). Our analysis documents generally high correlation values for the pair of IMF4 of ENSO BEST and PDO for any sliding-window size, suggesting a strong link between ENSO and PDO at this timescale, particularly between 1940 and the late 1960s, and between the mid 1990s and 2015 (Fig. 7). On the contrary, for the time interval between the late 1960s and 1985 correlation assumes relatively low values, especially for sliding-window sizes smaller than 40 years, suggesting that at this timescale ($\sim$5 y) the link between ENSO and PDO has weakened possibly due to other disturbances (Fig. 7).

The TDIC results for the pairs of IMF4, IMF6, and IMF7 of the normalized discharge anomaly (statistically significant IMFs for the time series from the hydrological station SA0693) and the climate indices for the time interval between 1940 and 2015 (ENSO BEST, SSN, and PDO) are summarized in Fig. 8. The outcomes for IMF3 with a mean period $\bar{T} \approx 1$ y (annual cycle), mainly controlled by the SAMS, are not shown.

For IMF4 (mean period $\bar{T} = 2.5$ y), until approximately 1980, the correlation between NQ and ENSO BEST showed a similar structure to that obtained by correlating NQ and PDO, with generally low correlation values (both positive and negative). After 1980, the ENSO BEST index continued to exhibit low correlation values with the normalized discharge anomaly. This result is also confirmed by analyzing the TDICC of the IMF4 pair of ENSO BEST and the normalized discharge anomaly at different time lags from 2 to 12 months (Supplementary information, Fig. S9). Conversely, the PDO was highly anti-correlated with the normalized discharge anomaly (Fig. 8). For short sliding window sizes (<10 y), until the early 1990s we also observed short time intervals ($\approx$5 y long) at approximately 15 y recurrence-time intervals, for which a strong positive correlation between the normalized discharge anomaly and both ENSO BEST and PDO was found. This behavior reflects that the frequencies of both IMF4 (e.g., of NQ and ENSO BEST) were nearly constant, with close, but different values, generating a quasi-periodic short time interval during which the two IMF4 were locally in phase (i.e., strongly correlated). We consider this an artifact produced by the method without any real physical meaning.

For IMF6 (mean period $\bar{T} = 9.4$ y) TDIC exhibited rather similar correlations between the pairs of the normalized discharge anomaly and ENSO BEST and PDO indices, respectively. Except for locally high positive values, especially for PDO at about 1980, relatively low correlation values were found until approximately 1990 and a strong anti-correlation afterwards. In contrast, SSN correlation with the normalized discharge anomaly resulted in a generally opposite behavior, with generally weak or negative values between approximately the mid-1960s and the early 1990s. A similar behavior was also found by analyzing the TDICC of the IMF6 pair of SSN and the normalized discharge anomaly with different time lags, except those for time lags>6 months larger positive correlation values were obtained (Supplementary information, Fig. S10).

For IMF7 (mean period $\bar{T} = 21.6$ y), the normalized discharge anomaly showed a generally strong positive correlation with
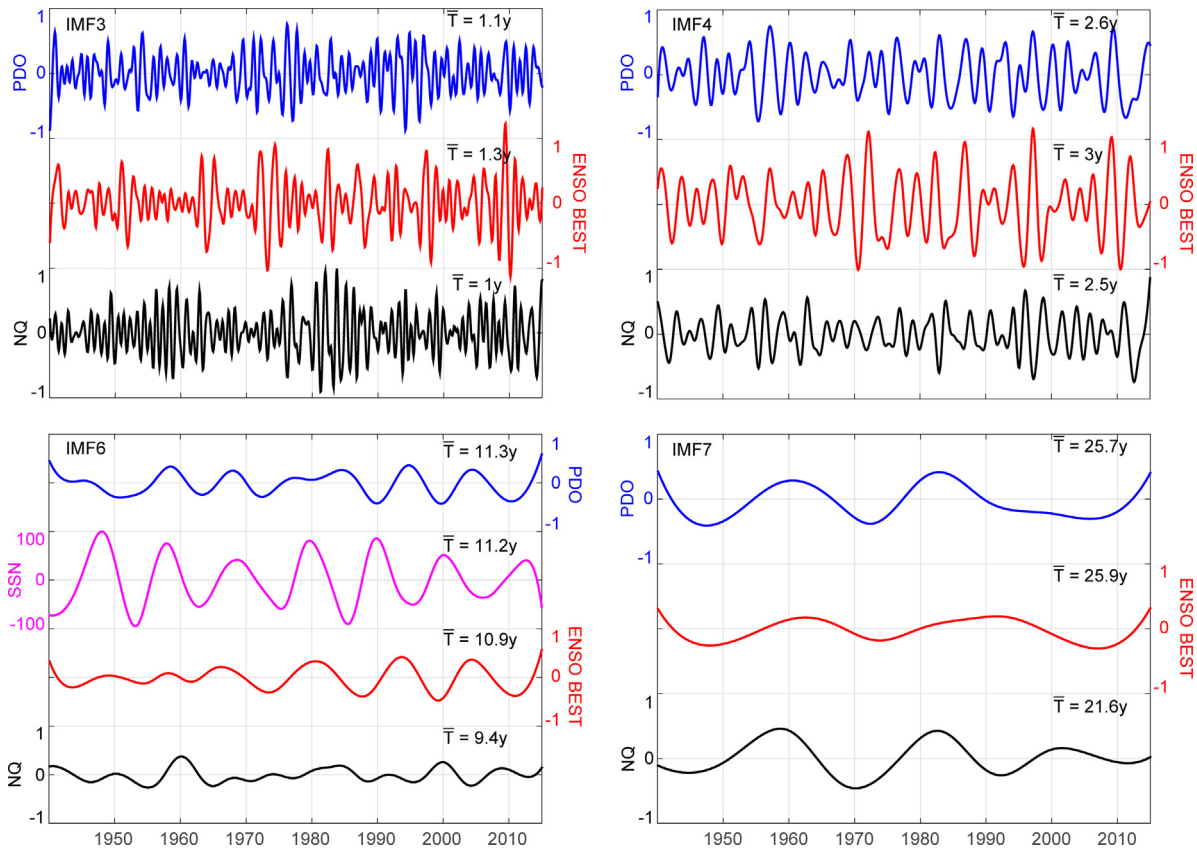
Fig. 6. EEMD results for the time interval between 1940 and 2015. Shown are each statistically significant IMF of NQ (black) (Table 3) and statistically significant IMFs of the used climate indices (ENSO BEST: red, PDO: blue, and SSN: magenta). The mean period $\bar{T}$ of each IMF is also indicated.
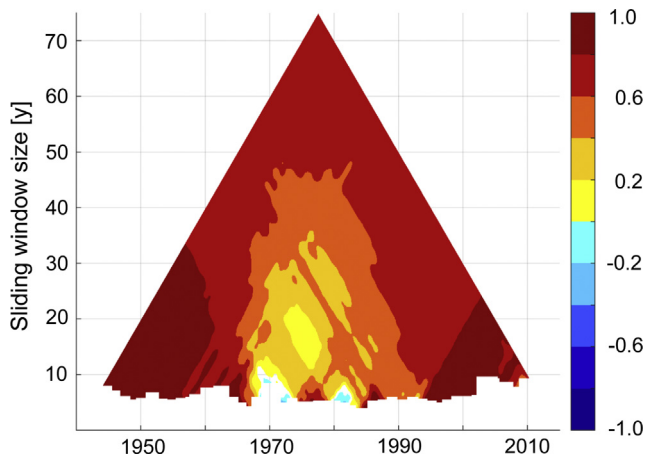

Fig. 7. Time-Dependent Intrinsic Correlation (TDIC) analysis of the correlation of IMF4 between ENSO BEST (mean period $\bar{T}$ = 5.8 y) and PDO (mean period $\bar{T}$ = 5.0 y) for the time interval from 1940 to 2015. The horizontal axis is the time of the series (i.e., from 1940 to 2015), where the current position indicates the center of the sliding window, and the vertical axis is the size of the sliding window. For each instant (i.e. month) for which the TDIC has to be estimated, the correlation between the two time series is calculated for different time-window sizes, defined by Eq. (11). Only statistically significant values (p < 0.05) are shown. Except for the time interval between approximately 1970 and 1990, a strong positive correlation is found for most sliding window sizes.

PDO. In comparison to NQ-PDO pair, ENSO BEST correlation with the normalized discharge anomaly generally resulted in smaller correlation values for IMF7. Finally, ENSO BEST and PDO indices exhibited strong correlations at all timescales, whereas SSN and

PDO showed a strong correlation until approximately 1980 and a strong anti-correlation since then (Supplementary information, Figs. S11 and S12).

4.2. Time interval from 1956 to 2015

For this time interval, four time series of the normalized discharge anomaly were available from different hydrological stations (JU0016, SA0604, SA0629, and SA0693). As for the time interval between 1940 and 2015, EEMD resulted in eight IMFs and one residue for all hydrological stations and the climate-indices time series (Table 5). For all time series of the normalized discharge anomaly, a monotonically increasing residue was obtained (Fig. 9). We observed that each time series of the normalized discharge anomaly was composed of a set of statistically significant IMFs which differ from the others in terms of the mean period $\bar{T}$, i.e. regarding the associated timescale (Table 5).

For example, the time series of NQ from station SA0604 exhibited one statistically significant IMF (IMF7, mean period $\bar{T}$ = 22.1 y), whereas from station SA0629 it presented two IMFs (IMF5 and IMF7, with mean period equal to 4.3 y and 23.3 y, respectively). Also, station JU0016 was associated with five statistically significant IMFs (IMF3-7) (Fig. 9). Furthermore, in case that different time series of NQ were composed of an IMF associated with the same timescale, the mean periods $\bar{T}$ had relatively close values (Table 5).

In addition, for the time interval between 1956 and 2015, the time series from station SA0693 revealed the same set of four IMFs as for the time interval between 1940 and 2015 (Tables 3 and 5). Importantly, we observed the local increase of the amplitude of the oscillations of IMF3 of NQ from the middle 1970s to the late 1990s. This was already discussed for the time interval between
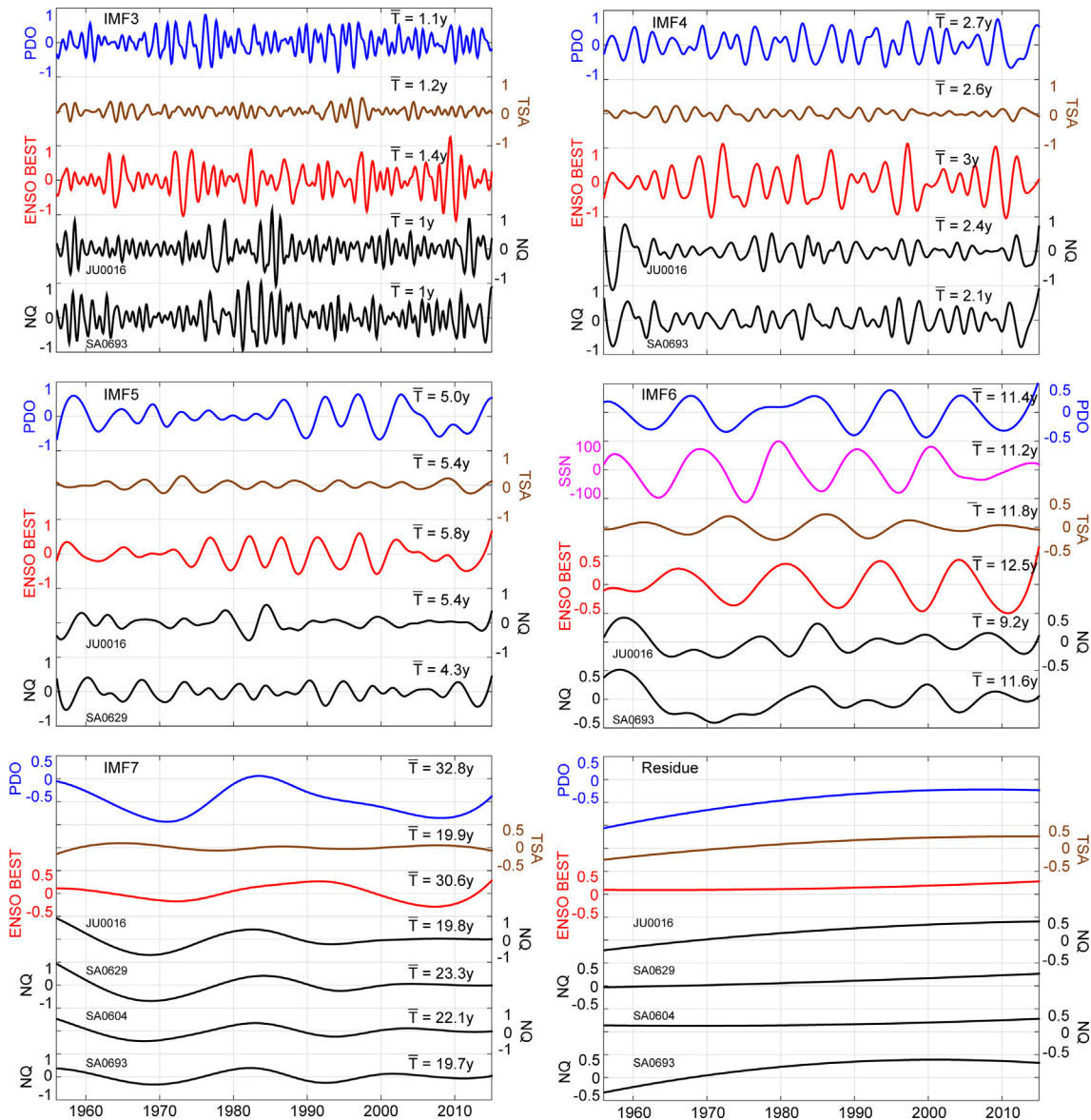
Fig. 8. TDIC results obtained from pairs of same order IMFs of normalized discharge anomaly of station SA0693 and the processed climate indices for the time interval between 1940 and 2015. Top: IMF4 ($\bar{T}$ = 2.5 y) matches between NQ and (left) ENSO BEST and (right) PDO. Middle: IMF6 ($\bar{T}$ = 9.4 y) matches between NQ and (left) ENSO BEST, (center) SST, and (right) PDO. Bottom: IMF7 ($\bar{T}$ = 21.6 y) matches between NQ and (left) ENSO BEST and (right) PDO. Only statistically significant values (p < 0.05) are shown.

1940 and 2015, in association with one period of oscillation of IMF7 (Fig. 9); in this case, the time series were not long enough to evaluate the same behavior for the time interval between the early 1950s and the middle 1960s. To a lesser degree, the IMF4 (~2.3 y) and IMF5 (~5 y) of NQ presented locally increased amplitudes of the oscillations from the middle 1970s to the late 1990s (Fig. 9). As for the time interval between 1940 and 2015, the instantaneous frequency associated with each IMF of the normalized discharge anomaly had approximately constant values around

the mean frequency value (see Supplementary information, Figs. S13-20).

Monthly time series of ENSO BEST, TSA, SSN, and PDO for this time interval were also analyzed using the EEMD (Table 5). It emerged that the ENSO BEST index was associated with five IMFs (IMF3-7), the SSN index with one IMF (IMF6), and the PDO index with six IMFs (IMF2-7). Note that for both ENSO BEST and PDO indices, the IMF7 presented less than two cycles during this time interval and, although statistically significant, results for these

Table 5
Summary of EEMD analysis for the normalized discharge anomaly NQ (hydrological station SA0693, SA0604, SA0629, JU0016), ENSO BEST, SSN, and PDO for the time interval 1956–2015. For each statistically significant IMF (p < 0.05), the value of its mean period $\bar{T}$ [y] is indicated; mean period values are indicated only for statistically significant IMFs; mean periods in parenthesis are associated with IMFs considered unreliable, although statistically significant, because their mean period is greater than half of a time-series length (i.e., less than three cycles occurred during the time interval of the time series).

	$\bar{T}$[y]							
	NQ SA0693	NQ SA0604	NQ SA0629	NQ JU0016	ENSO BEST	TSA	SSN	PDO
IMF1	–	–	–	–	–	–	–	–
IMF2	–	–	–	–	–	–	–	0.6
IMF3	1	–	–	1	1.4	1.2	–	1.1
IMF4	2.1	–	–	2.4	3	2.6	–	2.7
IMF5	–	–	4.3	5.4	5.8	5.4	–	5
IMF6	11.6	–	–	9.2	12.5	11.8	11.2	11.4
IMF7	19.7	22.1	23.3	19.8	(30.6)	19.9	–	(32.8)
IMF8	–	–	–	–	–	–	–	–

Fig. 9. EEMD results for the time interval between 1956 and 2015. For each statistically significant IMF of normalized discharge anomaly (Table 5), all relevant statistically significant IMFs of the available climate indices are shown. IMFs mean periods $\bar{T}$ are also indicated. The residue for each time series is also shown.

two indices of IMF7 could not be considered reliable. Furthermore, especially for the high frequency IMFs (IMF2-4), the climate indices showed approximately constant instantaneous frequency, except for local short and large oscillations around the mean frequency value. The outcomes of EEMD, Hilbert spectral analysis, and statistical significance testing are documented in the Supplementary information (Figs. S21–28).

For the original time series, the time-independent Pearson correlation analysis of the normalized discharge anomaly and each climate index showed generally low values (absolute correlation values lower than 0.14, Table 6). In the case of IMF pairs, time-independent Pearson correlation values remained small except for the IMF7 for station-to-station pairs or station-to-PDO pairs (Supplementary information, Table S1-5 for each IMF). Concerning

Table 6
Pearson correlation values between the normalized discharge anomaly (NQ) and the available climate indices for the time interval between 1956 and 2015, for the entire time series (TS). The Pearson correlation values for each IMF match are available in the Supplementary information (Tables S1-5). Only statistically significant correlation values are shown (p < .05).

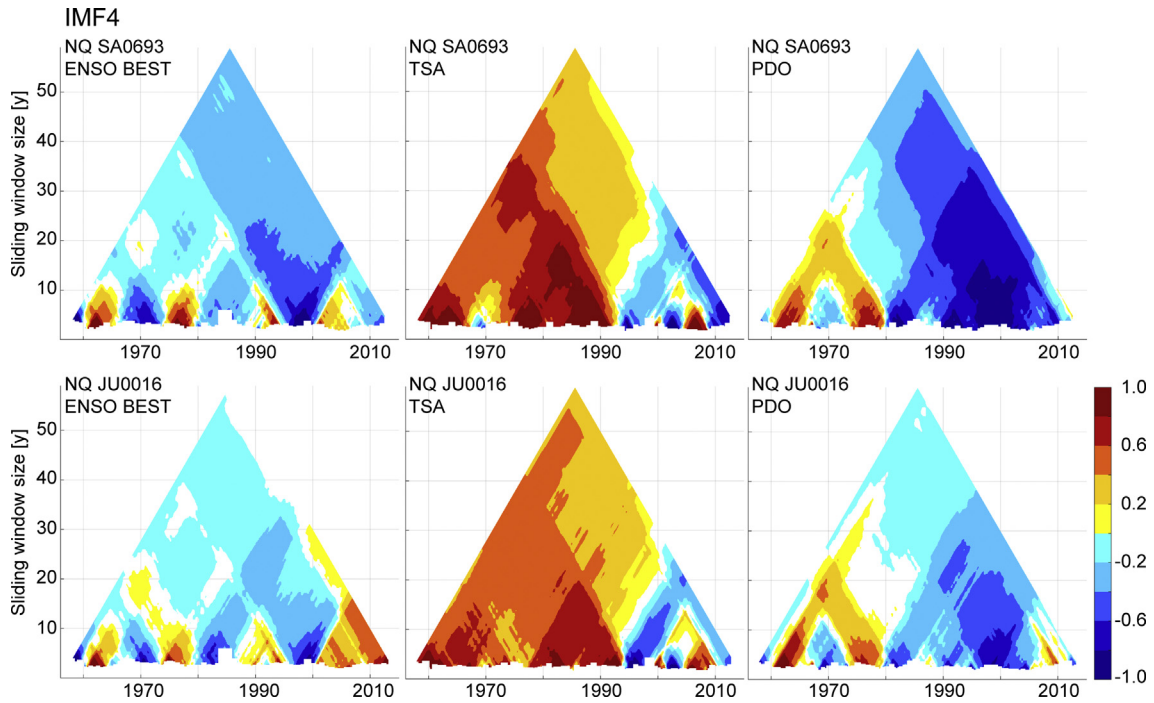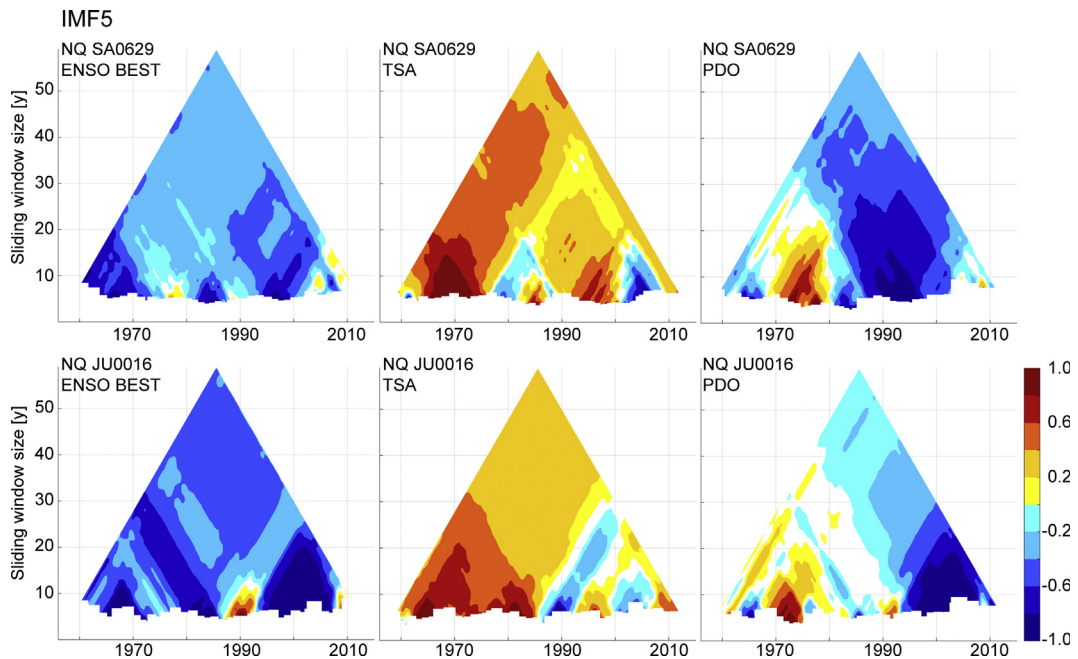|	NQ SA0604	NQ SA0629	NQ JU0016	ENSO BEST	TSA	SSN	PDO
NQ SA0693	0.782	0.740	0.623	–	0.124	–	–
NQ SA0604		0.709	0.501	–	0.083	0.140	–
NQ SA0629			0.580	–	0.107	0.140	–
NQ JU0016				–	0.127	–	0.094
ENSO BEST					−0.087	–	0.444
TSA						−0.288	–
SSN							–

Fig. 10. TDIC results obtained by matching IMF4 of normalized discharge anomaly from stations SA0693 and JU0016, and the available climate indices for the time interval from 1956 to 2015. Top: SA0693 ($\bar{T}$ = 2.1 y) matches between NQ and (left) ENSO BEST, (center) TSA, and (right) PDO. Bottom: JU0016 ($\bar{T}$ = 2.4 y) matches between NQ and (left) ENSO BEST (center) TSA, and (right) PDO.

the TDIC, we observed that for the IMF4 pairs ($\bar{T} \sim 2.3$ y), TDIC exhibited for short sliding window sizes (<10 y) a behavior similar to that observed for the time interval between 1940 and 2015 for ENSO and, limited to approximately 1980, for PDO correlations with NQ (Fig. 10). This behavior was due to the fact that the frequencies of both IMF4s (e.g., of NQ and ENSO BEST) were nearly constant, with close, but different values. This generated quasi-

periodic short-time intervals during which the two IMF4 were locally in phase (i.e., strongly correlated), but resulting to be weakly anti-correlated elsewhere. Importantly, these high positive correlation values cannot always be associated with positive or negative ENSO or PDO phases and, as for the time interval between 1940 and 2015, we consider them as an artifact produced by the method without any real physical meaning. Interestingly, for the

Fig. 11. TDIC results obtained by matching IMF5 of normalized discharge anomaly from stations SA0629 and JU0016, and the available climate indices for the time interval from 1956 to 2015. Top: SA0629 ($\bar{T}$ = 4.3 y) matches between NQ and (left) ENSO BEST, (center) TSA, and (right) PDO. Bottom: JU0016 ($\bar{T}$ = 5.4 y) matches between NQ and (left) ENSO BEST (center) TSA, and (right) PDO.

IMF4 pair of the normalized discharge anomaly and TSA index, both available time series of the normalized discharge anomaly (SA0693 and JU0016) exhibited very high correlation values until 1990, whereas after the middle 1990s, high heterogeneity was observed in TDIC. The analysis of TDICC of the IMF4 pair of TSA and the normalized discharge anomaly for both stations did not exhibit appreciable differences in the cross-correlation temporal structure up to four-month long time lag, whereas for time-lags >4 months generally smaller correlation values or high anti-correlation were found until approximately 1990 (Supplementary information, Figs. S29 and S30). On the contrary, for the pair of the normalized discharge anomaly and PDO index, TDIC showed strong anti-correlation for the time series from station SA0693 after approximately 1980.

For IMF5 ($\bar{T} \sim 5$ y), TDIC mostly exhibited a strong anti-correlation between the normalized discharge anomaly and the ENSO BEST index for both available time series (SA0629 and JU0016, Fig. 11). This result is also obtained applying the TDICC analysis to the IMF5 pair of ENSO BEST and the normalized discharge anomaly for both stations, revealing a strong anti-correlation up to six-month long time lag, whereas for time lags >6 months generally weaker anti-correlation was found (Supplementary information, Figs. S31 and S32).

The IMF5 pair of the normalized discharge anomaly and TSA index instead revealed generally high positive correlation values, especially between approximately 1960 and the middle 1980s for sliding-window sizes smaller than 20 y. In contrast, the IMF5 pairs of the normalized discharge anomaly and PDO index showed a weak relationship until 1990 but strong anti-correlation afterwards.

For IMF6 ($\bar{T} \sim 10$ y), pronounced heterogeneous results were observed for the hydrological stations SA0693 and JU0016 (Fig. 12). For the IMF6 pairs of the normalized discharge anomaly and both ENSO BEST and PDO indices, TDIC for the time series from station SA0693 mostly showed a structure of values opposite to that obtained for the IMF6 pairs of NQ and both TSA and SSN indices. There existed a relatively strong correlation until 1990 and a subsequent strong anti-correlation. For the time series from station JU0016 the correlation values between the normalized discharge anomaly and the climate indices was weaker, except for the IMF6 pair of the normalized discharge anomaly and SSN index, which exhibited a relatively high anti-correlation.

For IMF7 ($\bar{T} \sim 20$ y), although PDO evidenced strong correlation values for any available sliding window size, as it was observed between 1940 and 2015, these results could not be considered reliable, since less than two cycles were available for the time interval between 1956 and 2015. Instead, for this timescale ($\bar{T} \sim 20$ y) TDIC results for the pair of the normalized discharge anomaly and TSA index revealed a generally weaker relationship until the early 1980s compared to shorter timescales, showing negative values for all four stations, and rather high positive values starting from approximately 1990 (Fig. S33).

5. Discussion

The EEMD analysis proved to be an efficient method to document long-term river-discharge trends and to decipher magnitude and frequency of oscillatory modes of river-discharge variability at different timescales in the southern Central Andes of NW Argentina. In addition, the combination of EEMD and TDIC analyses provided important insights to help identify linkages with large-scale modes of climate variability that might have affected river discharge in NW Argentina between 1940 and 2015. The EEMD analysis showed for both analyzed time intervals (between 1940 and 2015, and 1956 and 2015) that all time series (i.e., five normalized discharge anomaly and four climate indices) could be considered as the combination of eight intrinsic mode functions (IMFs) associated with different mean periods and one residual. In the following sections, we first discuss the IMFs results and the associated implications of linking river discharge with large-scale modes of climate variability. In a second step, we address the residuals as long-term trends of river discharge for both considered time intervals, discussing them in a regional perspective.

5.1. IMFs

In our study the EEMD analysis resulted in four statistically significant IMFs for the time series of the normalized discharge anomaly from station SA0693, i.e. four IMFs components with physically meaningful information (Wu et al., 2004). This observation allows one to consider the obtained four IMFs as quasi-periodic modes of variability of the normalized discharge anomaly, which can be linked to large-scale modes of climate variability at similar time-
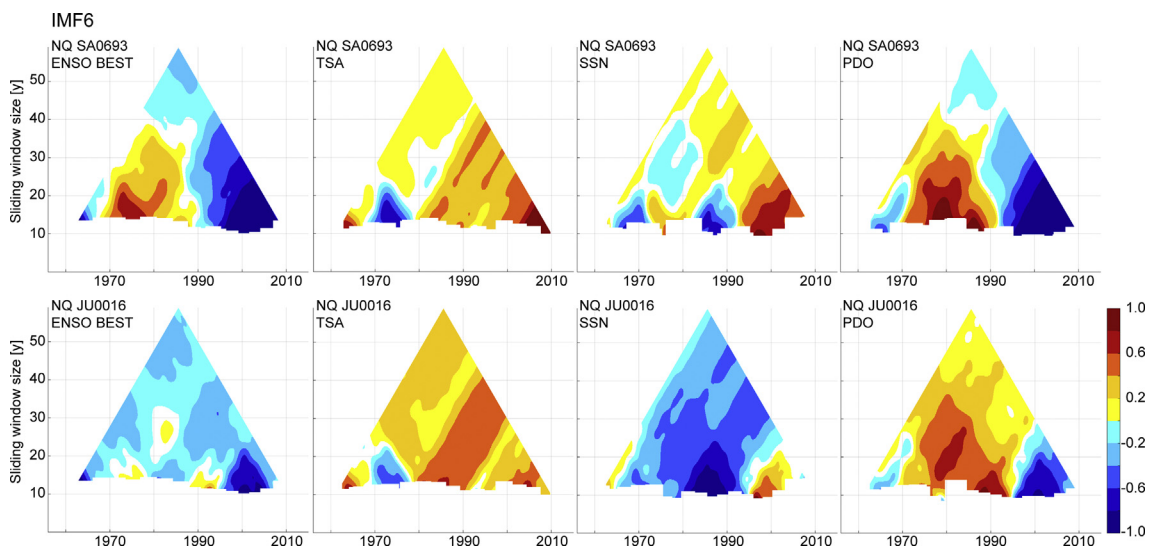

Fig. 12. TDIC results obtained by matching IMF6 of NQ of hydrological stations SA0693 and JU0016, and the available climate indices for the time interval from 1956 to 2015. Top: SA0693 ($\bar{T}$ = 11.6 y) matches between NQ and (left) ENSO BEST, (center-left) TSA, (center-right) SSN, and (right) PDO. Bottom: JU0016 ($\bar{T}$ = 9.2 y) matches between NQ and (left) ENSO BEST (center-left) TSA, (center-right) SSN, and (right) PDO.

scales (Antico and Kröhling, 2011; Antico and Torres, 2015; Massei and Fournier, 2012; Molina et al., 2015; Wang et al., 2015).

For station SA0693, the same statistically significant IMFs (IMF3, IMF4, IMF6, and IMF7) were obtained for both considered time intervals, with similar mean period values $\bar{T}$. Relatively small differences between $\bar{T}$ values of the same IMF obtained for the two time intervals were to be expected, given that the IMFs obtained by the EEMD method are approximations of the true envelope constituting the original time series (Wang et al., 2010). Therefore, results obtained from the analysis between 1940 and 2015 hold also true for the time interval between 1956 and 2015 when the time series was not long enough to allow for an analogous analysis.

The results of our study revealed furthermore that a complex system of climate and coupled atmosphere-ocean processes control river discharge variability in the southern Central Andes. This is due to the geographic setting of the study area at the transition between the tropics and subtropics, the pronounced topographic and climatic gradients, and the various factors controlling rainfall combined with different superposed atmospheric phenomena such as the SALLJ, SACZ, and mountain waves (Boers et al., 2015; Carvalho et al., 2012; de la Torre et al., 2015; de la Torre and Alexander, 2005; Vera et al., 2006).

Several studies in the past two decades have applied spectral analysis to discharge time series for different rivers in South America to associate large-scale climate modes of variability with discharge deviations for these regions (Antico et al., 2014; Antico and Kröhling, 2011; Antico and Torres, 2015; Apaéstegui et al., 2014; Compagnucci et al., 2014, 2000; García and Mechoso, 2005; Pasquini and Depetris, 2010, 2007; Poveda et al., 2001; Robertson and Mechoso, 1998; Stosic et al., 2016). Different methodologies have been applied, from the classical Fourier Transform (García and Mechoso, 2005; Pasquini and Depetris, 2010; Poveda et al., 2001; Robertson and Mechoso, 1998) to more complex techniques, such as wavelet analysis (Apaéstegui et al., 2014; Compagnucci et al., 2014, 2000; Pasquini and Depetris, 2007), permutation entropy and statistical complexity analysis (Stosic et al., 2016), and Empirical Mode Decomposition (EMD) (Antico et al., 2014; Antico and Kröhling, 2011; Antico and Torres, 2015; Molina et al., 2015). Below, we discuss our results in light of these previous findings, referring to the timescales on ~2 – 5 y, ~10 y, and ~20 y as the *multi-annual*, *decadal*, and *multi-decadal timescales*, respectively.

5.1.1. Multi-annual timescales (~2–5 y)

Some of the previous studies suggested that at multi-annual timescales much of the discharge variability of some major South American rivers (i.e., Uruguay, Paraná, Paraguay, Negro, La Plata, São Francisco) may be linked with ENSO activity (García and Mechoso, 2005; Pasquini and Depetris, 2007; Robertson and Mechoso, 1998; Stosic et al., 2016) and the North Atlantic Oscillation (NAO) (Antico et al., 2014; Hurrell et al., 2003). The role of ENSO as a potential driver of river-discharge variability was also documented by Compagnucci et al. (2000) for Argentine rivers in the Andes at about 35° S, and by Poveda et al. (2001) for most Colombian rivers.

The results of our study document a link between ENSO and the normalized discharge anomaly for two drainage basins (SA0629 and JU0016) at multi-annual timescales (~5 y) (i.e., positive ENSO phases were associated with lower river discharge and *vice versa*, Fig. 11). Accordingly, ENSO appears as a potential forcing factor for discharge variability at these timescales. At shorter timescales (~2 y), however, there appears to be a weak relationship between ENSO and the normalized discharge anomaly, even considering delays in response of up to 12 months (Figs. 9 and S9).

In contrast, at both ~2 y and 5 y timescales, anomalies in the Southern Tropical Atlantic ocean SST, characterized by the TSA index, exhibited a relatively strong link with discharge anomaly at least until 1990 (Fig. 10 and Fig. 11). Cross-correlation analysis would also suggest delay in response by a few months (<4) between variations of TSA and discharge (Supplementary information, Figs. S29 and S30). However, caution should be taken for the evaluation of the delay in response using the TDICC technique, given that the IMFs obtained by the EEMD method are approximations of the true envelope composing the original time series (Wang et al., 2010). The results obtained from the TDIC analysis between the TSA index and the normalized discharge anomaly are partly in agreement with previous findings, suggesting that SST anomalies in the tropical Atlantic control discharge in South American rivers at decadal to multi-decadal timescales (Antico and Torres, 2015; García and Mechoso, 2005). Interestingly, we observed that at multi-annual timescales, when the correlation between PDO and discharge was weak (before 1990), TSA had a strong correlation with the discharge anomaly. Conversely, when the correlation between PDO and discharge was stronger (after 1990), the link between TSA weakened. To our knowledge, no previous study has documented a similar observation. We infer that the PDO and SST anomaly of the southern tropical Atlantic alternately modulate discharge variability in rivers of the southern Central Andes (see below).

5.1.2. Decadal timescales (~10 y)

Recent studies have linked solar activity (i.e., sunspot number) and motion with multi-annual to decadal variations in streamflow of the Paraná river (Antico and Kröhling, 2011; Compagnucci et al., 2014) and subtropical Andean rivers up to 35° S lat (e.g., Compagnucci et al., 2014). Similar evidence coupled with SST anomalies of the southern tropical Atlantic emerged for the Amazon river (Antico and Torres, 2015). It was also suggested that the Atlantic SST anomaly is a driver for discharge variability in major South American rivers on both decadal and multi-decadal timescales (García and Mechoso, 2005; Pasquini and Depetris, 2010, 2007; Robertson and Mechoso, 1998).

With respect to solar activity, our results confirmed a strong link between SSN and TSA indices given by the relatively high anti-correlation values (IMF6, Fig. 9 and Supplementary information Table S4 and Fig. S34), as previously suggested by Antico and Torres (2015). Furthermore, only for the time series from station JU0016, whose catchment includes the climatic transition zone between the humid and semi-arid sectors of the eastern Andean flanks, we found a relatively strong anti-correlation between the normalized discharge anomaly and SSN until approximately until 1990. However, we did not identify a coherent spatial pattern that would have indicated an unambiguous influence of solar activity on river-discharge variability. This finding was corroborated by the results of the TSA analysis, which did not demonstrate a clear link between discharge variability and SST anomaly in the southern tropical Atlantic at these timescales. On the other hand, PDO impact on river discharge variability at decadal timescales appeared to become stronger compared to multi-annual timescales, i.e. associated with a strong correlation until 1990 and a strong anti-correlation afterwards.

5.1.3. Multi-decadal timescales (~20 y)

On multi-decadal timescales, PDO showed a particularly strong link with the discharge anomaly, resulting likely from a first-order control of discharge variability in the southern Central Andes (Fig. 8). This finding agrees with results obtained by Marengo (2009) and Marengo et al. (2012), who suggested that rainfall and discharge trends in the Amazon basin can be explained by multi-decadal modes of climate variability, such as PDO, for example. Similar results were found by Antico et al. (2014), who proposed a link at multi-decadal timescales between the Pacific ocean SST variability

and streamflow of the Paraná river in southeastern South America. However, instead of using the PDO index Antico et al. (2014) used the Interdecadal Pacific Oscillation index, which also includes southern Pacific SST changes (Parker et al., 2007).

5.2. Trends of normalized discharge anomaly and the 1976–77 climate shift

The EEMD method interprets the residual obtained from decomposing a time series as the long-term trend (Huang et al., 1998; Wu et al., 2007). For the normalized discharge anomaly (NQ), although with different magnitude, monotonically increasing, statistically significant trends were found for all hydrological stations and time intervals (Fig. 9). In particular, we observed that including or excluding the first 16 years of data from hydrological station SA0693 does not influence the character of the overall trends. In addition, the mean increase for both time intervals (from 1940 to 2015 and from 1956 to 2015) was approximately 10% of the standard deviation per decade. In a previous study, we evaluated trends of the same hydrological stations, using a different method based on standard and quantile regression on the time interval between 1940 and 1999, i.e. excluding the last 16 years (Castino et al., 2016). In that analysis we found a mean increase of the normalized discharge anomaly by approximately 8.5% per decade, which is in good agreement with the outcomes of this study. Similar results of long-term trend values obtained by different methods and different lengths of the time series (i.e., excluding or not excluding the first or last decades) demonstrates the robustness of these trend results for NQ.

In addition, Castino et al. (2016) documented a change point towards higher discharge values from 1971 to 1977 in agreement with previous studies (Compagnucci et al., 2000; García and Mechoso, 2005; García and Vargas, 1998; Genta et al., 1998; Robertson and Mechoso, 1998). These authors linked the rapid increase in river discharge in the southern Central Andes with the 1976–77 global climate shift (Carvalho et al., 2011; Graham, 1994; Jacques-Coper and Garreaud, 2015; Kayano et al., 2009; Marengo, 2009; Miller et al., 1994), highlighting an intensification of the hydrological cycle. Castino et al. (2016) furthermore documented a statistically significant decrease in discharge following the large increase corresponding with the change point, which already indicated an oscillatory component in the normalized discharge anomaly.

The EEMD results document that beginning with the middle 1970s to the early 1990s the amplitude of most modes of oscillation of discharge largely increased (see Sections 3.2.1 and 3.2.2). We hypothesize that this increase is linked to a multi-decadal PDO phase and, to a lesser degree, SST anomaly of the southern tropical Atlantic variability at multi-annual timescales, respectively. In particular, it can be noticed that the local increase in IMF3 (annual timescales) appeared to be synchronous with one period of oscillation of IMF7 (multi-decadal timescales) (Fig. 6). Since IMF3 represents the mode of oscillation mainly associated with the SAMS, one possible explanation is that the positive phase of PDO modulated the intensity of the SAMS, which in turn resulted in enhanced discharge on multi-decadal timescales.

Therefore, based on the results of the EEMD analysis, we hypothesize that the rapid increase in discharge observed between 1971 and 1977 (i.e., Castino et al., 2016) is likely due to the superposition of two distinct components: First, the oscillation rise of discharge variability at multi-decadal timescales between approximately 1970 and 1982, linked to a PDO phase change (Figs. 5 and 8); second, the long-term positive trend observed for the time interval 1940–2015. In addition, during the 1970s the amplitude of discharge variability was locally further intensified by the oscillations linked to TSA modes of variability on multi-annual timescales.

Partly similar explanations have been proposed by Zhang et al. (2016). These authors analyzed the multi-decadal trend towards wetter conditions in southeastern South America (SESA) during the 20th century, which was followed by a decadal-scale drying trend at the beginning of the 21st century. Castino et al. (2016) observed that the drying trend in the southern Central Andes already started in the early 1980s. However, despite some differences in the amplitude of the changes between model estimations and observations, Zhang et al. (2016) showed in their model-based study that the trend towards wetter conditions is likely driven by radiative forcing associated with increasing greenhouse gases, which could have caused the southward tropical expansion. SESA is located within the subtropical descending branch of the Hadley cell, which usually suppresses convection activity and forces dry conditions at the surface. According to Zhang et al. (2016), the southward tropical expansion would have moved the subtropical descending branch of the Hadley cell away from SESA, resulting in the increase in rainfall in SESA. Zhang et al. (2016) also proposed that the drying trends observed at the beginning of the 21st century are mainly attributable to internal climate variability, such as the Pacific Decadal Variability (PDV) (Mantua and Hare, 2002) and the Atlantic Multi-decadal Oscillation (AMO) (Enfield et al., 2001).

6. Conclusions

We analyzed trends and modes of oscillation of discharge anomaly from small to medium drainage basins (10^2–10^4 km^2) in the southern Central Andes of NW Argentina. These catchments are located in the transition between predominantly low-elevation, humid areas in the east to medium- and high-elevation semi-arid areas of the mountain belt in the west.

We relied on daily discharge observations and generated five time series of the monthly normalized discharge anomaly (NQ): one for the time interval between 1940 and 2015 (75 y), and four for the time interval between 1956 and 2015 (59 y).

In our analysis we applied the Hilbert-Huang Transform to the monthly NQ time series and obtained four key results:

1. Monotonically increasing, statistically significant trends were found for all hydrological stations and time intervals, although with different magnitude. This result agrees with similar findings of previous studies in this region, documenting an overall intensification of the hydrological cycle.

2. The Ensemble Empirical Mode Decomposition analysis revealed that discharge variability in this region can be described by five quasi-periodic, statistically significant oscillatory modes, with mean periods varying from 1 y to ∼20 y and different magnitude.

3. Discharge variability is mostly linked to Pacific Decadal Oscillation (PDO) phases at multi-decadal (∼20 y) timescales and, to a lesser degree, to the SST anomaly of the southern tropical Atlantic at multi-annual timescales. In addition, we observed that the PDO and SST anomaly of the southern tropical Atlantic might interfere by modulating discharge variability in rivers in the southern Central Andes, especially at multi-annual timescales. To a lesser degree, discharge variability also exhibited evidence for a link with ENSO and solar activity.

4. We hypothesize that the discharge change point observed between 1971 and 1977, and previously associated with the 1976–77 global climate shift, results from the combination of the periodic enhancement of discharge that occurred between the middle 1970s and the early 1990s and the long-term increasing trend. This appears to have been associated with the multi-decadal PDO phase and multi-annual variability of the SST anomaly of the southern tropical Atlantic (TSA).

Acknowledgements

Appendix A. Supplementary data

Supplementary data associated with this article can be found, in the online version, at https://doi.org/10.1016/j.jhydrol.2017.10.001.

References

Antico, A., Kröhling, D.M., 2011. Solar motion and discharge of Paraná River, South America: evidence for a link. Geophys. Res. Lett. 38, 1–5. https://doi.org/10.1029/2011GL048851.

Antico, A., Schlotthauer, G., Torres, M.E., 2014. Analysis of hydroclimatic variability and trends using a novel empirical mode decomposition: application to the Paraná River Basin. J. Geophys. Res. Atmos. 119, 1218–1233. https://doi.org/10.1002/2013JD020420.

Antico, A., Torres, M.E., 2015. Evidence of a decadal solar signal in the Amazon River: 1903 to 2013. Geophys. Res. Lett. 42. https://doi.org/10.1002/2015GL066089.

Apaéstegui, J., Cruz, F.W., Sifeddine, A., Vuille, M., Espinoza, J.C., Guyot, J.L., Khodri, M., Strikis, N., Santos, R.V., Cheng, H., Edwards, L., Carvalho, E., Santini, W., 2014. Hydroclimate variability of the northwestern Amazon Basin near the Andean foothills of Peru related to the South American Monsoon System during the last 1600 years. Clim. Past 10, 1967–1981. https://doi.org/10.5194/cp-10-1967-2014.

Bianchi, A.R., Yañez, C.E., 1992. Las precipitaciones en el Noroeste Argentino, Inst. Nac. Tecnol. Agropecu. Estacíon Exp.

Boers, N., Bookhagen, B., Marwan, N., Kurths, J., 2015. Spatiotemporal characteristics and synchronization of extreme rainfall in South America with focus on the Andes Mountain range. Dyn. Clim. https://doi.org/10.1007/s00382-015-2601-6.

Boers, N., Rheinwalt, A., Bookhagen, B., Barbosa, H.M.J., Marwan, N., Marengo, J.A., Kurths, J., 2014. The South American rainfall dipole: a complex network analysis of extreme events. Geophys. Res. Lett. 41, 7397–7405. https://doi.org/10.1002/2014GL061829.

Bookhagen, B., Burbank, D.W., 2010. Toward a complete Himalayan hydrological budget: spatiotemporal distribution of snowmelt and rainfall and their impact on river discharge. J. Geophys. Res. 115 (F3), F03019. https://doi.org/10.1029/2009JF001426.

Bookhagen, B., Strecker, M.R., 2012. Spatiotemporal trends in erosion rates across a pronounced rainfall gradient: examples from the southern Central Andes. Earth Planet. Sci. Lett. 327–328, 97–110. https://doi.org/10.1016/j.epsl.2012.02.005.

Bookhagen, B., Strecker, M.R., 2008. Orographic barriers, high-resolution TRMM rainfall, and relief variations along the eastern Andes. Geophys. Res. Lett. 35, L06403. https://doi.org/10.1029/2007GL032011.

Campetella, C.M., Vera, C.S., 2002. The influence of the Andes mountains on the South American low-level flow. Geophys. Res. Lett. 29, 1826. https://doi.org/10.1029/2002GL015451.

Carvalho, L.M.V., Jones, C., Liebmann, B., 2004. The south atlantic convergence zone: intensity, form, persistence, and relationships with intraseasonal to interannual activity and extreme rainfall. J. Clim. 17, 88–108.

Carvalho, L.M.V., Jones, C., Posadas, A.N.D., Quiroz, R., Bookhagen, B., Liebmann, B., 2012. Precipitation characteristics of the South American monsoon system derived from multiple datasets. J. Clim. 25, 4600–4620. https://doi.org/10.1175/JCLI-D-11-00335.1.

Carvalho, L.M.V., Jones, C., Silva, A.E., Liebmann, B., Silva Dias, P.L., 2011. The South American Monsoon System and the 1970s climate transition. Int. J. Climatol. 31, 1248–1256. https://doi.org/10.1002/joc.2147.

Castino, F., Bookhagen, B., Strecker, M.R., 2016. River-discharge dynamics in the Southern Central Andes and the 1976–77 global climate shift. Geophys. Res. Lett. 1–9. https://doi.org/10.1002/2016GL070868.

Cencetti, C., Rivelli, F.R., 2011. Landslides Dams Induced by Debris Flows in Quebrada Del Toro (Province of Salta, Argentina). In: 5th International Conference on Debris-Flow Hazards Mitigation: Mechanics. Pre- Diction and Assessment. Casa Editrice Università La Sapienza, Padua, Italy, pp. 645–650.

Chang, C.Y., Chiang, J.C.H., Wehner, M.F., Friedman, A.R., Ruedy, R., 2011. Sulfate aerosol control of tropical atlantic climate over the twentieth century. J. Clim. 24, 2540–2555. https://doi.org/10.1175/2010JCLI4065.1.

Chen, X., Wu, Z., Huang, N.E., 2010. The time-dependent intrinsic correlation based on the empirical mode decomposition. Adv. Adaptive Data Anal. https://doi.org/10.1142/S1793536910000471.

Clette, F., Svalgaard, L., Vaquero, J.M., Cliver, E.W., 2014. Revisiting the sunspot number: a 400-year perspective on the solar cycle. Space Sci. Rev. 186, 35–103. https://doi.org/10.1007/s11214-014-0074-2.

COBINABE, 2010. Generación y Transporte de Sedimentos en la Cuenca Binacional del Río Bermejo, 1. Recursos Naturales. 2. Recursos Hídricos. 3. Desarrollo Sustentable. Buenos Aires. 10.1007/s13398-014-0173-7.2.

Compagnucci, R.H., Berman, A.L., Velasco Herrera, V., Silvestri, G., 2014. Are southern South American Rivers linked to the solar variability? Int. J. Climatol. 34, 1706–1714. https://doi.org/10.1002/joc.3784.

Compagnucci, R.H., Blanco, S.A., Figliola, M.A., Jacovkis, P.M., 2000. Variability in subtropical Andean Argentinean Atuel river; a wavelet approach. Environmetrics 11, 251–269. https://doi.org/10.1002/(SICI)1099-095X(200005/06)11:3<251::AID-ENV405>3.0.CO;2-0.

de la Torre, A., Alexander, P., 2005. Gravity waves above Andes detected from GPS radio occultation temperature profiles: mountain forcing? Geophys. Res. Lett. 32, 1–4. https://doi.org/10.1029/2005GL022959.

de la Torre, A., Pessano, H., Hierro, R., Santos, J.R., Llamedo, P., Alexander, P., 2015. The influence of topography on vertical velocity of air in relation to severe storms near the Southern Andes Mountains. Atmos. Res. 156, 91–101. https://doi.org/10.1016/j.atmosres.2014.12.020.

Dunne, T., Mertes, K.L.A., 2007. Rivers. In: Veblen, T., Young, K., Orme, A.R. (Eds.), The Physical Geography of South America. Oxford University Press, pp. 76–90.

Enfield, D.B., Mestas-Nunez, A.M., 1999. How ubiquitous is the dipole relationship in tropical Atlantic sea surface temperatures? Res. J. Geophys. https://doi.org/10.1029/1998JC900109.

Enfield, D.B., Mestas-Nunez, A.M., Trimble, P.J., 2001. The Atlantic Multidecadal Oscillation and its relation to rainfall and river flows in the continental U.S. Geophys. Res. Lett. 28, 2077–2080. https://doi.org/10.1029/2000GL012745.

Ferrero, M.E., Villalba, R., De Membiela, M., Ferri Hidalgo, L., Luckman, B.H., 2015. Tree-ring based reconstruction of Río Bermejo streamflow in subtropical South America. J. Hydrol. 525, 572–584. https://doi.org/10.1016/j.jhydrol.2015.04.004.

Flandrin, P., Gonçalves, P., Rilling, G., 2004. Detrending and denoising with empirical mode decompositions. In: Proc. 12th Eur. Signal Process. Conf., pp. 1581–1584.

Franzke, C., 2012. Nonlinear trends, long-range dependence, and climate noise properties of surface temperature. J. Clim. 25, 4172–4183. https://doi.org/10.1175/JCLI-D-11-00293.1.

Frigo, M., Johnson, S.G., 2005. The design and implementation of FFTW3. Proc. IEEE 93, 216–231. https://doi.org/10.1109/JPROC.2004.840301.

Gandu, A., Geisler, J., 1991. A primitive equations model study of the effect of topography on the summer circulation over tropical South America. J. Atmos. Sci. 48, 1822–1836.

Gandu, A.W., Silva Dias, P.L., 1998. Impact of tropical heat sources on the South American tropospheric upper circulation and subsidence. J. Geophys. Res. https://doi.org/10.1029/97JD03114.

García, N.O., Mechoso, C.R., 2005. Variability in the discharge of South American rivers and in climate/Variabilité des débits de rivières d'Amérique du Sud et du climat. Hydrol. Sci. J. 50, 37–41. https://doi.org/10.1623/hysj.50.3.459.65030.

García, N.O., Vargas, W.M., 1998. The temporal climatic variability in the "Rio de la Plata" Basin displayed by the river discharges. Clim. Change 38, 359–379. https://doi.org/10.1023/A:1005386530866.

Garreaud, R., Vuille, M., Clement, A.C., 2003. The climate of the Altiplano: observed current conditions and mechanisms of past changes. Palaeogeogr. Palaeoclimatol. Palaeoecol. 194, 5–22. https://doi.org/10.1016/S0031-0182(03)00269-4.

Garreaud, R.D., 2009. The Andes climate and weather. Adv. Geosci. 22, 3–11.

Garreaud, R.D., Molina, A., Farias, M., 2010. Andean uplift, ocean cooling and Atacama hyperaridity: A climate modeling perspective. Earth Planet. Sci. Lett. 292, 39–50. https://doi.org/10.1016/j.epsl.2010.01.017.

Genta, J.L., Perez-Iribarren, G., Mechoso, C.R., 1998. A recent increasing trend in the streamflow of rivers in southeastern South America. J. Clim. 11, 2858–2862.

Graham, N.E., 1994. Decadal-scale climate variability in the tropical and North Pacific during the 1970s and 1980s: observations and model results. Clim. Dyn. 10, 135–162. https://doi.org/10.1007/BF00210626.

Halloy, S., 1982. Contribucíon al estudio de la zona de Huaca huasi, Cumbres Calchaquíes (Tucumán Argentina). Univ. Nac, Tucumán.

Hoover, K.D., 2003. Nonstationary time series, cointegration, and the principle of the common cause. Br. J. Philos. Sci. 54, 527–551. https://doi.org/10.1093/bjps/54.4.527.

Huang, N.E., 2005. Introduction to the hilbert huang transform. Transform 5, 1–26. doi:10.1142/9789812703347_0001.

Huang, N.E., Shen, S.S.P., 2014. Hilbert-Huang transform and its applications. World Scientific Publishing, Singapore.

Huang, N.E., Shen, Z., Long, S.R., 1999. A new view of nonlinear water waves: the Hilbert Spectrum 1. Annu. Rev. Fluid Mech. 31, 417–457. https://doi.org/10.1146/annurev.fluid.31.1.417.

Huang, N.E., Shen, Z., Long, S.R., Wu, M.C., Shih, H.H., Zheng, Q., Yen, N.-C., Tung, C.C., Liu, H.H., 1998. The empirical mode decomposition and the Hilbert spectrum for nonlinear and non-stationary time series analysis. Proc. R. Soc. A Math. Phys. Eng. Sci. 454, 903–995. https://doi.org/10.1098/rspa.1998.0193.

Huang, N.E., Wu, M.-L.C., Long, S.R., Shen, S.S.P., Qu, W., Gloersen, P., Fan, K.L., 2003. A confidence limit for the empirical mode decomposition and Hilbert spectral analysis. Proc. R. Soc. A Math. Phys. Eng. Sci. 459, 2317–2345. https://doi.org/10.1098/rspa.2003.1123.

Huang, N.E., Wu, Z., 2009. Ensemble empirical mode decomposition: a noise-assisted data analysis method. Adv. Adapt. Data Anal. 1, 1. https://doi.org/10.1142/S1793536909000047.

Huang, N.E., Wu, Z., Long, S.R., Arnold, K.C., Chen, X., Blank, K., 2009. On instantaneous frequency. Adv. Adapt. Data Anal. 1, 177–229. https://doi.org/10.1142/S1793536909000096.

Huang, Y., Schmitt, F.G., 2014. Time dependent intrinsic correlation analysis of temperature and dissolved oxygen time series using empirical mode decomposition. J. Mar. Syst. 130, 90–100. https://doi.org/10.1016/j.jmarsys.2013.06.007.

Hurrell, J.W., Kushnir, Y., Ottersen, G., 2003. An overview of the North Atlantic oscillation. Clim. Significance Environ. Impact 1–35. https://doi.org/10.1029/134GM01.

Jacques-Coper, M., Garreaud, R.D., 2015. Characterization of the 1970s climate shift in South America. Int. J. Climatol. 35, 2164–2179. https://doi.org/10.1002/joc.4120.

Jeffery, M.L., Yanites, B.J., Poulsen, C.J., Ehlers, T.A., 2014. Vegetation-precipitation controls on Central Andean topography. J. Geophys. Res. Earth Surf. 119, 1354–1375. https://doi.org/10.1002/2013JF002919.

Kayano, M.T., Pestrelo de Oliveira, C., Andreoli, R.V., 2009. Interannual relations between South American rainfall and tropical sea surface temperature anomalies before and after 1976. Int. J. Climatol. 29, 1439–1448. https://doi.org/10.1002/joc.1824.

Khaliq, M.N., Ouarda, T.B.M.J., Ondo, J.C., Gachon, P., Bobée, B., 2006. Frequency analysis of a sequence of dependent and/or non-stationary hydro-meteorological observations: a review. J. Hydrol. 329, 534–552. https://doi.org/10.1016/j.jhydrol.2006.03.004.

Labat, D., Ronchail, J., Callede, J., Guyot, J.L., Oliveira, E. De, Guimarães, W., 2004. Wavelet analysis of Amazon hydrological regime variability. Geophys. Res. Lett. 31, L02501. https://doi.org/10.1029/2003GL018741.

Lliboutry, L., 1998. Glaciers of Chile and Argentina. In: Williams, R.S., Ferrigno, J. (Eds.), Glaciers of South Amrica USGS Professional Paper 1386-I. USGS, Denver, pp. 109–206.

Mantua, N., Hare, S., 2002. The Pacific decadal oscillation. J. Oceanogr. 58, 35–44.

Marcato, G., Bossi, G., Rivelli, F., Borgatti, L., 2012. Debris flood hazard documentation and mitigation on the Tilcara alluvial fan (Quebrada de Humahuaca, Jujuy province, North-West Argentina). Nat. Hazards Earth Syst. Sci. 12, 1873–1882. https://doi.org/10.5194/nhess-12-1873-2012.

Marcato, G., Pasuto, A., Rivelli, F.R., 2009. Mass movements in the Rio Grande Valley (Quebrada de Humahuaca, Northwestern Argentina): a methodological approach to reduce the risk. Adv. Geosci. 22, 59–65.

Marengo, J.A., 2009. Long-term trends and cycles in the hydrometeorology of the Amazon basin since the late 1920s. Hydrol. Process. 23, 3236–3244. https://doi.org/10.1002/hyp.7396.

Marengo, J.A., 2004. Interdecadal variability and trends of rainfall across the Amazon basin. Theor. Appl. Climatol. 78, 79–96. https://doi.org/10.1007/s00704-004-0045-8.

Marengo, J.A., Liebmann, B., Grimm, A.M., Misra, V., Silva Dias, P.L., Cavalcanti, I.F.A., Carvalho, L.M.V., Berbery, E.H., Ambrizzi, T., Vera, C.S., Saulo, A.C., Nogues-Paegle, J., Zipser, E., Seth, A., Alves, L.M., 2012. Recent developments on the South American monsoon system. Int. J. Climatol. 32, 1–21. https://doi.org/10.1002/joc.2254.

Massei, N., Fournier, M., 2012. Assessing the expression of large-scale climatic fluctuations in the hydrological variability of daily Seine river flow (France) between 1950 and 2008 using Hilbert-Huang Transform. J. Hydrol. 448–449, 119–128. https://doi.org/10.1016/j.jhydrol.2012.04.052.

Mcleod, A.I., Gweon, H., 2013. Optimal deseasonalization for geophysical time series. J. Environ. Stat. 4, 1–11.

Melack, J.M., Novo, E.M.L.M., Forsberg, B.R., Piedade, M.T.F., Maurice, L., 2009. Floodplain ecosystem processes. Geophys. Monogr. Ser. 186.

Miller, A., Cayan, D., Barnett, T., Graham, N., Oberhuber, J., 1994. The 1976–77 climate shift of the Pacific Ocean. Oceanography 7, 21–26. https://doi.org/10.5670/oceanog.1994.11.

Molina, A., Vanacker, V., Brisson, E., Mora, D., Balthazar, V., 2015. Multidecadal change in streamflow associated with anthropogenic disturbances in the tropical Andes. Hydrol. Earth Syst. Sci. 19, 4201–4213. https://doi.org/10.5194/hess-19-4201-2015.

Nourani, V., Komasi, M., Mano, A., 2009. A multivariate ANN-wavelet approach for rainfall-runoff modeling. Water Resour. Manage. 23, 2877–2894. https://doi.org/10.1007/s11269-009-9414-5.

Parker, D., Folland, C., Scaife, A., Knight, J., Colman, A., Baines, P., Dong, B., 2007. Decadal to multidecadal variability and the climate change background. J. Geophys. Res. Atmos. 112, 1–18. https://doi.org/10.1029/2007JD008411.

Pasquini, A.I., Depetris, P.J., 2010. ENSO-triggered exceptional flooding in the Paraná River: where is the excess water coming from? J. Hydrol. 383, 186–193. https://doi.org/10.1016/j.jhydrol.2009.12.035.

Pasquini, A.I., Depetris, P.J., 2007. Discharge trends and flow dynamics of South American rivers draining the southern Atlantic seaboard: an overview. J. Hydrol. 333, 385–399. https://doi.org/10.1016/j.jhydrol.2006.09.005.

Poveda, G., Jaramillo, A., Gil, M.M., Quiceno, N., Mantilla, R.I., 2001. Seasonality in ENSO-related precipitation, river discharges, soil moisture, and vegetation index in Colombia. Water Resour. Res. 37, 2169–2178. https://doi.org/10.1029/2000WR900395.

Robertson, A.W., Mechoso, C.R., 1998. Interannual and decadal cycles in river flows of southeastern South America. J. Clim. 11, 2570–2581.

Rodó, X., Rodríguez-Arias, M.Á., 2006. A new method to detect transitory signatures and local time/space variability structures in the climate system: The scale-dependent correlation analysis. Clim. Dyn. 27, 441–458. https://doi.org/10.1007/s00382-005-0106-4.

Rohmeder, W., 1943. Observaciones meterológicas en la región encumbrada de las Sierras de Famatina y del Aconquija (republica Argentina). An. Soc. Cient. Arg. 136, 97–124.

Ruthsatz, B., 1977. Pflanzengesellschaften und ihre Lebensbedingun¬gen in den Andinen Halbwüsten Nordwest-Argentiniens. Diss. Bot. 39.

Salio, P., Nicolini, M., Saulo, A.C., 2002. Chaco low-level jet events characterization during the austral summer season. J. Geophys. Res. Atmos. 107, 4816. https://doi.org/10.1029/2001JD001315.

Schwerdtfeger, W., 1976. Climates of Central and South America – World Surv. Climatol. – Vol. 12. Elsevier Sci., New York.

Seluchi, M., Saulo, A., 2003. The northwestern Argentinean low: a study of two typical events. Mon. Weather, 2361–2378.

da Silva, A., de Carvalho, L., 2007. Large-scale index for South America Monsoon (LISAM). Sci. Lett. Atmos. https://doi.org/10.1002/asl.

Smith, C.A., Sardeshmukh, P.D., 2000. The effect of ENSO on the intraseasonal variance of surface temperatures in winter. Int. J. Climatol. 20, 1543–1557. doi:10.1002/1097-0088(20001115)20:13<1543::AID-JOC579>3.0.CO;2-A.

Stosic, T., Telesca, L., de Souza Ferreira, D.V., Stosic, B., 2016. Investigating anthropically induced effects in streamflow dynamics by using permutation entropy and statistical complexity analysis: a case study. J. Hydrol. 540, 1136–1145. https://doi.org/10.1016/j.jhydrol.2016.07.034.

Torrence, C., Compo, G.P., 1998. A practical guide to wavelet analysis. Bull. Am. Meteorol. Soc. 79, 61–78. https://doi.org/10.1175/1520-0477(1998) 079<0061: APGTWA>2.0.CO;2.

Vera, C., Higgins, W., Amador, J., Ambrizzi, T., Garreaud, R., Gochis, D., Gutzler, D., Lettenmaier, D., Marengo, J.A., Mechoso, C.R., Nogues-Paegle, J., Silva Dias, P.L., Zhang, C., 2006. Toward a unified view of the American monsoon systems. J. Clim. https://doi.org/10.1175/JCLI3896.1.

Vuille, M., Keimig, F., 2004. Interannual variability of summertime convective cloudiness and precipitation in the central Andes derived from ISCCP-B3 data. J. Clim. 17, 3334–3348.

Wang, G., Chen, X.-Y., Qiao, F.-L., Wu, Z., Huang, N.E., 2010. On intrinsic mode function. Adv. Adapt. Data Anal. 2, 277–293. https://doi.org/10.1142/S1793536910000549.

Wang, T., Zhang, M., Yu, Q., Zhang, H., 2012. Comparing the applications of EMD and EEMD on time-frequency analysis of seismic signal. J. Appl. Geophys. 83, 29–34. https://doi.org/10.1016/j.jappgeo.2012.05.002.

Wang, Chau, W. chuan, Xu, K. wing, Chen, D. meiX.Y., 2015. Improving forecasting accuracy of annual runoff time series using ARIMA based on EEMD decomposition. Water Resour. Manage. 29, 2655–2675. https://doi.org/10.1007/s11269-015-0962-6.

Wilcox, L.J., Highwood, E.J., Dunstone, N.J., 2013. The influence of anthropogenic aerosol on multi-decadal variations of historical global climate. Environ. Res. Lett. 8, 24033. https://doi.org/10.1088/1748-9326/8/2/024033.

Wilks, D.S., 1995. Statistical methods in the atmospheric sciences. An introduction.

World Meteorological Organization, 2011. Guide to Climatological Practices WMO-No. 100, WMO. ed. WMO, Geneva.

Wu, Z., Huang, N.E., 2009. Ensemble empirical mode decomposition: a noise assisted data analysis method. Adv. Adapt. Data Anal. 1, 1–41. https://doi.org/10.1142/S1793536909000047.

Wu, Z., Huang, N.E., Long, S.R., Peng, C.-K., 2007. On the trend, detrending, and variability of nonlinear and nonstationary time series. Proc. Natl. Acad. Sci. U. S. A. 104, 14889–14894. https://doi.org/10.1073/pnas.0701020104.

Wu, Z., Huang, N.E., Wallace, J.M., Smoliak, B.V., Chen, X., 2011. On the time-varying trend in global-mean surface temperature. Clim. Dyn. 37, 759–773. https://doi.org/10.1007/s00382-011-1128-8.

Wu, Z., Huang, N.E., Zhaohua, B.W., 2004. A study of the characteristics of white noise using the empirical mode decomposition method. Proc. R Soc. A Math. Phys. Eng. Sci. 460, 1597–1611. https://doi.org/10.1098/rspa.2003.1221.

Wu, Z., Schneider, E.K., Kirtman, B.P., Sarachik, E.S., Huang, N.E., Tucker, C.J., 2008. The modulated annual cycle: An alternative reference frame for climate anomalies. Clim. Dyn. 31, 823–841. https://doi.org/10.1007/s00382-008-0437-z.

Zeiler, A., Faltermeier, R., Tome', A., Keck, I., Puntonet, C., Brawanski, A., Lang., E., 2013. Sliding empirical mode decomposition-brain status data analysis and modeling. In: Georgieva, P., Mihaylova, L., Jain, L.C. (Eds.), Advances in Intelligent Signal Processing and Data Mining. pp. 311–349.

Zhang, H., Delworth, T.L., Zeng, F., Vecchi, G., Paffendorf, K., Jia, L., 2016. Detection, attribution and projection of regional rainfall changes on (multi-) decadal time scales: a focus on southeastern South America. J. Clim. https://doi.org/10.1175/JCLI-D-16-0287.1. JCLI-D-16-0287.1.

Zhang, Y., Yan, R., Gao, R.X., Feng, Z., 2010. Performance enhancement of ensemble empirical mode decomposition. Mech. Syst. Signal Process. 24, 2104–2123. https://doi.org/10.1016/j.ymssp.2010.03.003.

Zhou, J., Lau, K.-M., 1998. Does a monsoon climate exist over South America? J. Clim. 11, 1020–1040.